

Gravity-driven coatings on curved substrates: a differential geometry approach

Pier Giuseppe Ledda^{1,2,†}, M. Pezzulla³, E. Jambon-Puillet⁴, P.-T. Brun⁴ and F. Gallaire¹

¹Laboratory of Fluid Mechanics and Instabilities, École Polytechnique Fédérale de Lausanne, CH-1015 Lausanne, Switzerland

²Dipartimento di Ingegneria Civile, Ambientale e Architettura, University of Cagliari, 09123 Cagliari, Italy

³Slender Structures Lab, Department of Mechanical and Production Engineering, Århus University, Inge Lehmanns Gade 10, 8000 Århus C, Denmark

⁴Department of Chemical and Biological Engineering, Princeton University, Princeton, NJ 08540, USA

(Received 23 February 2022; revised 26 August 2022; accepted 28 August 2022)

Drainage and spreading processes in thin liquid films have received considerable attention in the past decades. Yet, our understanding of three-dimensional cases remains sparse, with only a few studies focusing on flat and axisymmetric substrates. Here, we exploit differential geometry to understand the drainage and spreading of thin films on curved substrates, under the assumption of negligible surface tension and hydrostatic gravity effects. We develop a solution for the drainage on a local maximum of a generic substrate. We then investigate the role of geometry in defining the spatial thickness distribution via an asymptotic expansion in the vicinity of the maximum. Spheroids with a much larger (respectively smaller) height than the equatorial radius are characterized by an increasing (respectively decreasing) coating thickness when moving away from the pole. These thickness variations result from a competition between the variations of the substrate's slope and mean curvature. The coating of a torus presents larger thicknesses and a faster spreading on the inner region than on the outer region, owing to the different curvatures in these two regions. In the case of an ellipsoid with three different axes, spatial modulations in the drainage solution are observed as a consequence of a faster drainage along the short principal axis, faithfully reproduced by a three-dimensional asymptotic solution. Leveraging the conservation of mass, an analytical solution for the average spreading front is obtained. The solutions are in agreement with numerical simulations and experimental measurements obtained from the coating of a curing polymer on diverse substrates.

Key words: thin films, lubrication theory, gravity currents

† Email address for correspondence: pier.ledda@epfl.ch

1. Introduction

Coating flows are found in many environmental, chemical and engineering processes (Weinstein & Ruschak 2004), such as spin coating (Scriven 1988; Schwartz & Roy 2004) and dip coating (Landau & Levich 1942). Additionally, coating assisted fabrication methodologies recently showed potential in the fabrication of curved spherical shells (Lee *et al.* 2016) and inflatable soft tentacles (Jones *et al.* 2021). The plethora of observed coating patterns motivated a great deal of studies aimed at understanding the underlying physical mechanisms (Weinstein & Ruschak 2004). Typical examples include inertia-driven Kapitza waves (Kapitza 1948; Kapitza & Kapitza 1965), Marangoni effects due to gradients in surface tension (Oron 2000; Hosoi & Bush 2001; Scheid 2013; Xue, Pack & Stone 2020) and the formation of drops (Rayleigh 1882; Taylor 1950; Fermigier *et al.* 1992; Chandrasekhar 2013; Jambon-Puillet *et al.* 2021) and rivulets (Lerisson *et al.* 2019, 2020; Ledda *et al.* 2020; Ledda & Gallaire 2021) below horizontal and inclined substrates. Such formation of elongated structures along the streamwise direction is also typical of contact-line-driven instabilities, often called fingering, and occurs when a fluid spreads on a dry substrate (Oron, Davis & Bankoff 1997; Kondic 2003; Weinstein & Ruschak 2004; Craster & Matar 2009). Such patterns are identified as the physical origin for several geological structures such as stalactites (Short *et al.* 2005; Camporeale & Ridolfi 2012) and flutings in limestone caves (Camporeale 2015; Bertagni & Camporeale 2017; Ledda *et al.* 2021) and due to solidification and melting of water (Camporeale 2015), while physical or chemical erosion leads to scallops (Meakin & Jamtveit 2010) or linear karren (Bertagni & Camporeale 2021) patterns. Gravity currents, widely encountered in environmental fluid dynamics, are flows driven by gravity differences typically imputed to the presence of one phase heavier than the other which spreads on a substrate. Examples typically involve complex rheologies (Balmforth *et al.* 2000; Balmforth, Craster & Sassi 2002; Balmforth *et al.* 2006) and include oil spreading on the sea (Hoult 1972), lava (Balmforth *et al.* 2000) and pyroclastic flows due to a volcano eruption, dust storms, avalanches (Simpson 1982; Huppert 1986; Balmforth & Kerswell 2005; Huppert 2006), slurry and sheet flows (Ancey 2007).

The analysis of spreading of currents requires the knowledge of the position, velocity and thickness of the advancing front. If the inertia of the flow is negligible, the dominant balance to describe the viscous gravity current is given by viscosity and buoyancy. With the aim of comparing their results with those of Keulegan (1957), Huppert & Simpson (1980) investigated the two-dimensional viscous gravity current on a horizontal substrate, driven by hydrostatic gravity effects. By combining a lubrication approximation with the volume conservation, the authors determined a self-similar solution for the thickness and spreading front, recovering the result of Smith (1969) in the case of the release of an initial amount of fluid. The general problem for different initial and boundary conditions, such as continuous feeding (Didden & Maxworthy 1982; Huppert 1982*b*), was investigated by Gratton & Minotti (1990) via a phase-plane formalism. When the substrate is inclined, a gravity component parallel to the substrate is introduced, which often dominates the dynamics. Huppert (1982*a*) highlighted that the lubrication solution at the leading order presents a discontinuity at the front, as long as surface tension and hydrostatic pressure gradients along the film are neglected. The thickness distribution far from the front is recovered by only considering the drainage along the in-plane directions of the substrate, so-called drainage solution (Huppert 1982*a*). For the inclined plane case, the thickness solution far from the front reads $h \propto x^{1/2}t^{-1/2}$ and is formally analogous to the result of Jeffreys (1930). The mathematical derivation may be more involved when the substrate is curved, e.g. in the case of the release of an initial volume of fluid on the outer side of a cone

Gravity-driven coatings on curved substrates

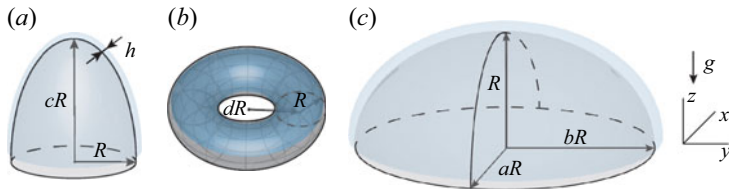


Figure 1. Different coated substrates considered in this work: (a) spheroid, (b) torus, (c) ellipsoid.

(Acheson 1990), a cylinder or a sphere (Takagi & Huppert 2010; Lee *et al.* 2016; Balestra *et al.* 2019) or in the inside of a downward-pointing cone or a sphere (Lin, Dijksman & Kondic 2021; Xue & Stone 2021).

From now on, we focus on the diverging spreading on a curved substrate away from the pole, while gravity points downwards (Takagi & Huppert 2010; Lee *et al.* 2016; Balestra *et al.* 2019), see figure 1. In this case, the drainage solution fairly reproduces the experimental observations since the hydrostatic pressure gradient due to the gravity component orthogonal to the substrate does not induce any instability of the thin film free surface. Takagi & Huppert (2010) studied the drainage and spreading on a cylinder and a sphere, in the vicinity of the pole. The drainage thickness scales as $h \sim t^{-1/2}$ both for the cylinder and the sphere. More refined drainage solutions were obtained by Balestra *et al.* (2019) and Lee *et al.* (2016) for the cylinder and the sphere, respectively. In both cases, an increase of the thickness moving from the pole to the equator is observed. However, as highlighted by the numerical simulations of Duruk, Boujo & Sellier (2021), the coating of an oblate spheroid with ratio between height and equatorial radius of 0.5 shows a decreasing thickness moving from the pole to the equator.

The latter example shows the effect of the substrate geometry in the resulting thickness distribution which stems from drainage induced by gravity. We therefore aim at exploring the role of the substrate in this process, which still needs to be systematically studied, even in the simple case of axisymmetric substrates. When the symmetry of the substrate is broken, spatial non-uniformities may also modify the picture previously described and require further investigation. Despite the abundance of studies on spreading in different conditions, the problem of three-dimensional drainage and spreading has been the object of limited studies on flat substrates (Lister 1992; Xue & Stone 2020), to the best of our knowledge. The role of the substrate in inducing three-dimensional drainage still needs to be assessed.

A lubrication model for generic substrates was developed in Roy, Roberts & Simpson (2002) and Howell (2003) by considering a generic orthogonal local coordinate system. The same result was obtained by Thiffeault & Kamhawi (2006) via classical differential geometry where the equations are written in the natural, local (general) coordinates system, not necessarily orthogonal. General coordinates define a local coordinate system, with the advantage of deriving general equations that can be used for any geometry and without the need of defining principal directions. The literature about the topic is extremely vast; for our purposes, the essential tools can be found in Deserno (2004) and Irgens (2019).

The lubrication equation in general coordinates offers the yet unexplored opportunity to systematically study the three-dimensional drainage and spreading on complex substrates through analytical solutions. In this work, we develop analytical solutions and approximations for the drainage and spreading problem on several substrates, with the aim of identifying relevant features of coatings on curved substrates. In the spirit of Huppert (1982a), we consider the case in which the tangential gravity components dominate the film thickness dynamics and we neglect the hydrostatic pressure and surface tension

effects, keeping only the leading-order terms given by the drainage gravity components. This approach is suitable to obtain simple analytical expressions to shed light on the leading effect of the substrate on the thickness distribution. The paper is organized as follows. In § 2, we introduce the coating problem of a generic substrate and the differential geometry tools necessary to understand the flow configuration. We then obtain a general solution in the vicinity of a local maximum of a diverging substrate. The following sections focus on how geometry influences the drainage around local maxima using the geometries reported in figure 1. Section 3 is devoted to the study of the drainage and spreading on a spheroid, where we show that, depending on the aspect ratio, the film can either get thicker or thinner as we move away from the pole. Subsequently, § 4 studies the problem of non-symmetric drainage and spreading on a torus. We conclude by studying the spatially non-uniform drainage and spreading solution on ellipsoids, in § 5. Eventually, the analytical and numerical results are compared with experimental measurements.

2. The coating problem of a generic substrate

2.1. Problem definition and metric terms in general coordinates

In this section, we introduce the essential differential geometry tools to solve the problem of the coating on a generic substrate. For a complete description of differential geometry and general coordinates, we refer to Deserno (2004). The derivation of the lubrication equation for generic curved substrates can be found in Roy *et al.* (2002), Thiffeault & Kamhawi (2006) and Wray, Papageorgiou & Matar (2017). The geometry is sketched in figure 2. We consider a generic substrate h^0 , on which lies a fluid film of thickness h , and introduce a Cartesian reference frame (x, y, z) . The substrate is identified by the position vector $\mathbf{X}(x^{(1)}, x^{(2)})$, where $(x^{(1)}, x^{(2)})$ denote the local coordinates used to parameterize the surface (e.g. the zenith and the azimuth for spherical coordinates, the radial coordinate and the azimuth for a cone). The flow equations are solved in the local and natural reference frame of the substrate. We introduce the local coordinate vectors parallel to the substrate $\mathbf{e}_i = \partial_i \mathbf{X}$, $i = 1, 2$ (not necessarily orthonormal), and the normal coordinate vector $\mathbf{e}_3 = \mathbf{e}_1 \times \mathbf{e}_2 / |\mathbf{e}_1 \times \mathbf{e}_2|$. From the knowledge of the local coordinate vectors, we introduce the 2×2 symmetric metric tensor components G_{ij} and the square root of the determinant of the metric on the substrate w , which is related to the area element on the surface dA through $dA = w dx^{(1)} dx^{(2)}$

$$G_{ij} = \mathbf{e}_i \cdot \mathbf{e}_j = G_{ji}, \quad w = (\det G_{ij})^{1/2}. \quad (2.1a,b)$$

The metric tensor defines the generic line element ds as $ds^2 = G_{11}(dx^{(1)})^2 + 2G_{12} dx^{(1)} dx^{(2)} + G_{22}(dx^{(2)})^2$. Therefore, the dimensions of each component depend on the considered parameterization $(x^{(1)}, x^{(2)})$, so that each part that composes ds^2 has the dimensions of the square of a length. We also introduce the second fundamental form and the curvature tensor, which respectively read, following Einstein's notation for the summation

$$S_{ij} = \partial_i \mathbf{e}_j \cdot \mathbf{e}_3, \quad K_i^{(j)} = S_{ik} G^{(kj)}, \quad (2.2a,b)$$

where $G^{(ij)}$ are the inverse metric tensor components, i.e. $G^{(ij)} = G_{ij}^{-1}$. The mean \mathcal{K} and the Gaussian \mathcal{G} curvatures read $\mathcal{K} = \text{tr } \mathbf{K}$ and $\mathcal{G} = \det \mathbf{K}$, respectively. A generic vector \mathbf{f} can be written in terms of its covariant and contravariant base, i.e. $\mathbf{f} = f^{(i)} \mathbf{e}_i = f_i \mathbf{e}^{(i)}$, where $\mathbf{e}^{(i)}$ is the covector defined as $\mathbf{e}^{(i)} \cdot \mathbf{e}_j = \delta_{ij}$. The two contravariant components, parallel to the substrate, of the gravity vector read $g_i^{(i)} = \mathbf{g} \cdot \mathbf{e}^{(i)}$, while the normal one reads

Gravity-driven coatings on curved substrates

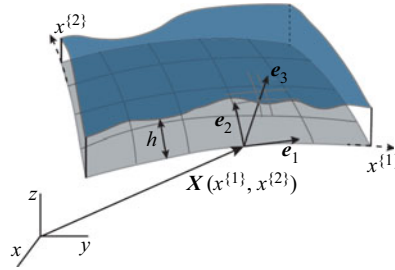


Figure 2. Sketch of the coordinate systems employed in this analysis. A global Cartesian reference frame (x, y, z) is considered. At each point, the position of the substrate is identified by the vector \mathbf{X} , which depends on the chosen parameterization $(x^{(1)}, x^{(2)})$ of the substrate. The derivatives of the position vector identify the local reference frame on the substrate, on which the lubrication equation is solved.

$g_3 = \mathbf{g} \cdot \mathbf{e}_3$. The gradient of a scalar function f and the divergence of a generic vector $\mathbf{f} = f^{(i)} \mathbf{e}_i$ respectively read (Irgens 2019)

$$\nabla f = \partial_i f G^{(ij)} \mathbf{e}_j = \partial^{(i)} f \mathbf{e}_j, \quad \nabla \cdot \mathbf{f} = w^{-1} \partial_i (w f^{(i)}). \quad (2.3a,b)$$

The above-defined quantities and differential operators are enough to describe the coating problem on a generic substrate, introduced in the following section.

2.2. Lubrication equation and drainage solution

We consider a thin viscous film, flowing on a substrate h^0 , of thickness h measured along the direction perpendicular to the substrate itself. The constant fluid properties are the density ρ , viscosity μ and the surface tension coefficient γ . In the absence of inertia, the lubrication model for a generic curved substrate was first derived by Roy *et al.* (2002) via central manifold theory. We non-dimensionalize the thickness with h_i and the tangential directions with R , i.e. a characteristic film thickness (e.g. the initial one, if uniform) and a relevant length of the substrate (e.g. its equatorial radius), respectively. We introduce the drainage time scale $\tau = \mu R / (\rho g h_i^2)$. Upon non-dimensionalization, the equation in coordinate-free form reads (Roy *et al.* 2002; Howell 2003; Roberts & Li 2006; Thiffeault & Kamhawi 2006)

$$\begin{aligned} (1 - \delta \mathcal{K} h + \delta^2 \mathcal{G} h^2) \frac{\partial h}{\partial t} + \frac{1}{3Bo} \nabla \cdot \left[h^3 \left(\nabla \tilde{\kappa} - \frac{\delta}{2} h (2\mathcal{K} \mathbf{I} - \mathbf{K}) \cdot \nabla \mathbf{K} \right) \right] \\ + \frac{1}{3} \nabla \cdot \left[h^3 \left(\mathbf{g}_t - \delta h \left(\mathcal{K} \mathbf{I} + \frac{1}{2} \mathbf{K} \right) \cdot \mathbf{g}_t + \delta g_3 \nabla h \right) \right] = 0, \end{aligned} \quad (2.4)$$

where $\tilde{\kappa} = \mathcal{K} + \delta(\mathcal{K}^2 - 2\mathcal{G})h + \delta \nabla^2 h$ is the free-surface curvature, $Bo = (\rho g R^2) / \gamma$ is the Bond number, $\delta = h_i / R$ is the aspect ratio of the thin film and \mathbf{g}_t and g_3 identify the gravity vector components tangential and normal to the substrate, respectively. The terms in the first and second brackets represent the flux induced by capillary and gravity effects, respectively. Capillary flow is induced, at leading order, by variations of the mean curvature of the substrate \mathcal{K} and leads to film thinning and thickening in the neighbourhood of local maximum and minimum values of the curvature (Roy *et al.* 2002). Corrections at order $O(\delta)$ introduce (i) free-surface curvature variations and (ii) higher-order terms of the substrate curvature. Gravity-induced fluxes are instead related, at leading order, by the gravity components tangential to the substrate \mathbf{g}_t . Corrections at $O(\delta)$ introduce hydrostatic

pressure gradients along the thin film. This equation can be written in compact form as follows:

$$(1 - \delta\mathcal{K}h + \delta^2\mathcal{G}h^2) \frac{\partial h}{\partial t} + \frac{1}{3} \nabla \cdot \mathbf{q} = 0, \tag{2.5}$$

so-called conservation form, where $\mathbf{q} = q^{(1)}\mathbf{e}_1 + q^{(2)}\mathbf{e}_2$ is the flux. The so-called drainage problem relies on two assumptions. The Bond number is assumed to be very large, i.e. $R^2/\ell_c^2 \gg 1$, where $\ell_c = \sqrt{\gamma/(\rho g)}$ is the capillary length. After this first assumption, the problem accounts only for gravity effects resulting from drainage and hydrostatic pressure gradients. The latter terms are important when the aspect ratio $\delta = h_i/R$ is not negligible, i.e. for a thick film on a large substrate (compared with the capillary length) with small radius of curvature (compared with the film thickness). A limit case occurs when the substrate is locally flat. The leading-order solution is given by the hydrostatic pressure terms, since drainage is absent. A case in which both capillary and hydrostatic effects cannot be neglected occurs instead when the radius of curvature of the substrate is comparable to the film thickness, i.e. regions of extremely large curvature such as the tip of a cone. In the following, we restrict ourselves to the situation in which the film is very thin and the substrate does not present regions of extremely large curvature. Therefore, also $\delta \ll 1$ is considered and the drainage problem reads

$$\frac{\partial h}{\partial t} + \frac{1}{3} \nabla \cdot [h^3 \mathbf{g}_t] = 0. \tag{2.6}$$

In this case, the flux per unit length is defined as $\mathbf{q} = q^{(1)}\mathbf{e}_1 + q^{(2)}\mathbf{e}_2 = h^3 g_t^{(1)}\mathbf{e}_1 + h^3 g_t^{(2)}\mathbf{e}_2$. The solution of the drainage problem requires only the knowledge of w and the tangential gravity vector components $g_t^{(i)}$.

The numerical implementation of the lubrication equation (2.4) is performed in the finite-element solver COMSOL Multiphysics, in which the lubrication equation is implemented in its conservation form (2.5). Quadratic Lagrangian elements are exploited for the numerical discretization, while the time marching is performed with the built-in backward differentiation formula (BDF) solver. In the case of (2.4), we solve for the variables $(h, \tilde{\kappa})$. We refer to the corresponding sections for more detail about the boundary conditions for the different substrates.

The validation procedure consists of a first mesh size validation. We thus verify the faithfulness of the employed parameterization $\mathbf{X}(x^{(1)}, x^{(2)})$ by a comparison with the parameterization $\mathbf{X} = (x, y, h^0(x, y))$, so-called Monge parameterization (Thiffeault & Kamhawi 2006; Mayo *et al.* 2015), reported in the electronic supplementary material (ESM available at <https://doi.org/10.1017/jfm.2022.758>) together with the other parameterizations employed in this work. We also verify the non-dimensionalization by solving the dimensional version of (2.4) and comparing the solution for each substrate with the non-dimensional model. To illustrate and complement the theoretical results, we finally compare in § 6 the drainage problem results with experiments performed following the procedure outlined in Lee *et al.* (2016) and Jones *et al.* (2021), for diverse substrates.

2.3. Asymptotic theory – general expression for the thickness at a local maximum

The employed substrate-free expression of the lubrication equation is suitable for analytical results. In this section, we develop a general expression for the thickness at a local maximum of the substrate. In the vicinity of the local maximum, the smooth substrate is described through a Monge parameterization of the substrate, i.e. $(x^{(1)} = x, x^{(2)} = y)$,

see the ESM for further detail. The generic substrate position vector in the vicinity of the maximum reads $\mathbf{X} = (x, y, h^0(x, y))$. The square root of the determinant of the metric tensor w and the tangential gravity components respectively read

$$w = \sqrt{1 + (\partial_x h^0)^2 + (\partial_y h^0)^2}, \quad g_t^{(1)} = -\frac{\partial_x h^0}{w^2}, \quad g_t^{(2)} = -\frac{\partial_y h^0}{w^2}. \quad (2.7a-c)$$

We expand the drainage solution in the vicinity of the maximum identified by the point $\mathbf{x} = (x, y) = \mathbf{0}$ by employing an asymptotic expansion in the spatial variables, i.e.

$$h(x, y, t) = H_0(t) + H_{11}(t)x + H_{12}(t)y + \dots \quad (2.8)$$

Upon substitution of the decomposition (2.8) in (2.6), the $O(1)$ problem for $H_0(t)$ reads

$$\begin{aligned} \frac{H'_0}{H_0^3} &= \left. \frac{(\partial_{xx} h^0 (1 + (\partial_y h^0)^2) - 2\partial_x h^0 \partial_{xy} h^0 \partial_y h^0 + \partial_{yy} h^0 ((\partial_x h^0)^2 + 1))}{3((\partial_y h^0)^2 + (\partial_x h^0)^2 + 1)^2} \right|_{\mathbf{x}=\mathbf{0}} \\ &= - \left(\frac{1}{3} (\mathbf{g} \cdot \mathbf{e}_3) \mathcal{K} \right) \Big|_{\mathbf{x}=\mathbf{0}}, \end{aligned} \quad (2.9)$$

with the initial condition $H_0(0) = 1$ in the case of a unitary initial thickness. At the maximum location, $\partial_x h^0 = \partial_y h^0 = 0$, i.e. the normal vector and gravity are aligned. Therefore, the quantity $(\frac{1}{3} (\mathbf{g} \cdot \mathbf{e}_3) \mathcal{K})|_{\mathbf{x}=\mathbf{0}}$ simplifies to $\partial_{xx} h^0 + \partial_{yy} h^0 = -\mathcal{K}_p$, where \mathcal{K}_p is the opposite of the mean curvature at the maximum. The resulting problem and associated solution read

$$\frac{H'_0(t)}{H_0(t)^3} = -\frac{1}{3} \mathcal{K}_p \rightarrow H_0(t) = \frac{1}{\sqrt{\frac{2\mathcal{K}_p t}{3} + 1}}. \quad (2.10)$$

A general expression for the drainage in the vicinity of a local maximum is obtained. Note that the mean curvature at the local maximum is negative, and thus $\mathcal{K}_p > 0$. The thickness at a local maximum depends on the mean curvature. From a geometrical point of view, the mean curvature represents variations of the tangential vectors along the surface. Since the normal to the surface and the gravity vector are aligned, the mean curvature determines the evolution of the tangential components of the gravity field, in the vicinity of the local maximum. In particular, an increase of \mathcal{K}_p implies larger values of gravity in the tangent plane of the substrate moving away from the pole and thus a faster drainage and a lower thickness, and *vice versa*. This solution allows one to identify the limits of the considered drainage model. If $\mathcal{K}_p = 0$, i.e. a locally flat substrate, there is no drainage and, therefore, the thickness is constant and equal to $H_0 = 1$. In this case, hydrostatic effects cannot be neglected since they are the leading-order effect and lead to a time-dependent drainage (Huppert & Simpson 1980). Therefore, the drainage model is not suitable to describe locally flat substrates. A second limiting case occurs when $\mathcal{K}_p \rightarrow \infty$, i.e. the radius of curvature in the vicinity of the local maximum tends to zero. A classical example is the tip of a cone, parameterized with the radius $x^{(1)} = r$ and the azimuth $x^{(2)} = \varphi$. In this case, an exact solution $h \propto \sqrt{r}$ is obtained (see the ESM), which presents a zero thickness at the pole, in accordance with solution (2.10), which tends to zero as $\mathcal{K}_p \rightarrow \infty$. In that case, hydrostatic and capillary effects are crucial to define the thickness distribution in the vicinity of the tip. Another important limitation comes from the considered geometry. When the fluid is located below the substrate, the

solution is formally analogous to (2.10), and predicts a progressive thinning. However, it is well known, in these situations, that hydrostatic pressure gradients and capillary effects play a key role since the Rayleigh–Taylor instability can occur (Balestra, Nguyen & Gallaire 2018*b*). In the case of converging geometries with a local minimum, the solution is formally analogous, but with $\mathcal{K}_p < 0$. In this case, the thickness progressively increases and tends to infinity for $t = -3/(2\mathcal{K}_p) > 0$, long after hydrostatic and capillary effects should have been considered. These combined effects contribute indeed to the Rayleigh–Taylor instability when the fluid lies below the substrate and for a levelling and flattening of the interface when it lies above.

Turning back to the situation where $\mathcal{K}_p > 0$ and remains finite, one can take the limit for $t \gg 1$ of solution (2.10), leading to

$$H_0(t) = \frac{1}{\sqrt{\frac{2\mathcal{K}_p t}{3}}} + O\left(\frac{1}{t^{3/2}}\right), \tag{2.11}$$

i.e. the solution is independent of the initial condition. This result is in agreement with the analysis in Lee *et al.* (2016), where the authors theoretically and experimentally showed an insensitivity of the film thickness with respect to the initial conditions.

In the following, we investigate the spatial evolution of the thin film thickness when moving away from the pole. We initially consider the case of an axisymmetric substrate, the spheroid.

3. Drainage and spreading on axisymmetric substrates: coating of a spheroid

3.1. Drainage problem

In this section, we consider the drainage of a thin film flowing on an spheroidal substrate of equatorial radius R (i.e. $a = b = 1$) and height cR . We non-dimensionalize the in-plane directions and substrate variables with the equatorial radius R . We parameterize the spheroidal surface via the zenith (or colatitude) $x^{(1)} = \vartheta$ and the azimuth $x^{(2)} = \varphi$

$$\mathbf{X}(\vartheta, \varphi) = (\sin \vartheta \cos \varphi, \sin \vartheta \sin \varphi, c \cos \vartheta). \tag{3.1}$$

A complete description of the metric and curvature tensors is reported in the ESM. The gravity term $g_t^{(1)}$ and w are

$$g_t^{(1)}(\vartheta) = \frac{c \sin(\vartheta)}{c^2 \sin^2(\vartheta) + \cos^2(\vartheta)}, \quad w(\vartheta) = \frac{1}{\sqrt{2}} \sin(\vartheta) \sqrt{(1 - c^2) \cos(2\vartheta) + 1 + c^2}, \tag{3.2a,b}$$

while $g_t^{(2)} = 0$. In the case $c = 1$, we recover the evolution equation for the spherical case, reported in the ESM. Following the previous section, we consider as initial condition a constant thickness on the substrate, i.e. $h(\vartheta, 0) = 1$. The problem is solved through an asymptotic expansion in the vicinity of the pole. We expand the solution at different orders in ϑ

$$h(\vartheta, t) = H_0(t) + \vartheta^2 H_2(t) + \vartheta^4 H_4(t) + \vartheta^6 H_6(t) + \dots \tag{3.3}$$

We introduce this ansatz and expand in powers of ϑ . At each order $O(\vartheta^n)$, one obtains an ordinary differential equation for H_n . The problem at orders $O(1)$ and $O(\vartheta^2)$ together with

their solution read

$$\left. \begin{aligned} \frac{2}{3}cH_0^3 + H_0' &= 0, \quad H_0(0) = 1 \rightarrow H_0 = \left(\frac{4ct}{3} + 1\right)^{-1/2}, \\ \left(\frac{2c}{3} - c^3\right)H_0^3 + 4cH_0^2H_2 + H_2' &= 0, \quad H_2(0) = 0, \\ \rightarrow H_2 &= \frac{(3c^2 - 2)(64\sqrt{3}c^3t^3 + 144\sqrt{3}c^2t^2 + 108\sqrt{3}ct + 27(\sqrt{3} - \sqrt{4ct + 3}))}{10(4ct + 3)^{7/2}}. \end{aligned} \right\} \quad (3.4a,b)$$

Applying the same procedure at orders $O(\vartheta^4)$ and $O(\vartheta^6)$, the solution up to $O(\vartheta^6)$ and at leading order for $t \gg 1$, reads (see Appendix A for further detail)

$$\begin{aligned} h(\vartheta, t) &= \sqrt{\frac{3}{4t}} \frac{1}{\sqrt{c}} \left(1 + \frac{1}{10} (3c^2 - 2) \vartheta^2 - \frac{(336c^4 - 408c^2 + 31) \vartheta^4}{4800} \right. \\ &\quad \left. + \frac{(58464c^6 - 115368c^4 + 62667c^2 - 4576) \vartheta^6}{1584000} \right) + O(\vartheta^8) + O\left(\frac{1}{t^{3/2}}\right). \end{aligned} \quad (3.6)$$

Note that the $O(1)$ large-time solution is formally analogous to (2.10) with $\mathcal{K}_p = 2c$, i.e. the opposite of the mean curvature at the pole.

We perform numerical simulations of (2.6), in the region $0 < \vartheta < \pi/2$. Owing to the hyperbolic nature of the equation, no boundary conditions are necessary at $\vartheta = 0$ and $\vartheta = \pi/2$, and thus we impose only the initial condition $h(\vartheta, 0) = 1$. Numerical convergence is achieved with the characteristic element size $\Delta\vartheta = 1^\circ$. Figure 3 shows a comparison of the numerical solution of (2.6) at $t = 100$ with the analytical ones at orders $O(\vartheta^2)$ (solid lines) and $O(\vartheta^6)$ (dashed lines), which shows an overall agreement. The solution at order $O(\vartheta^6)$ gives a better agreement with the numerics in a larger range of ϑ . For $c > 1.2$, the numerical and analytical solutions start to deviate for $\vartheta > 60^\circ$. The agreement with the solution at second order is good in most cases for $\vartheta < 60^\circ$. The second-order term in (3.6) vanishes when $c^* = \sqrt{2/3} \approx 0.81$. Under these conditions, the solution at $O(\vartheta^2)$ is constant along the zenith. The approximation at order $O(\vartheta^6)$ does not admit a constant solution. However, the minimum variation of its integral in the region $0 < \vartheta < \pi/2$, with respect to the constant value given by employing $H_0(t)$, is obtained for $c \approx 0.74$. Independently of the considered order of the solution, for very small (respectively very large) values of c the thickness decreases (respectively increases) when moving away from the pole. Moreover, for $c < c^*$, the numerical solution and the analytical one at order $O(\vartheta^6)$ present a non-monotonic behaviour, as shown in figure 3 for $c = 0.4, 0.6$, with an initial decrease followed by a slight increase for $\vartheta > 70^\circ$. The solutions for $c > c^*$ monotonically increase.

The leading-order large-time analytical solution presents a temporal decay $h \sim t^{-1/2}$. The spherical case is recovered by imposing $c = 1$ (Couder *et al.* 2005; Lee *et al.* 2016; Qin, Xia & Gao 2021). The large-time solution is independent of the initial thickness h_i . It is interesting to note the good agreement between the analytical and numerical solutions for $c < 1.2$ and $\vartheta > 1$, which is out of the expected range of validity of the asymptotic expansion. The relative size of the terms in the asymptotic expansion decreases as higher orders are considered, thus suggesting that the power series expansion may converge to the exact solution in the considered range of ϑ .

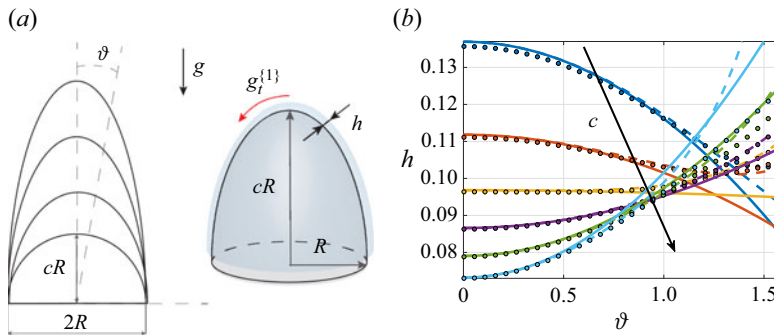


Figure 3. (a) Sketch of the spheroidal substrate with varying c . (b) Comparison of the numerical solution at $t = 100$ of (2.6) (coloured dots) with the analytical ones at order $O(\vartheta^2)$ (solid lines) and $O(\vartheta^6)$ (dashed lines). Different colours identify different values of c : $c = 0.4$ (blue), $c = 0.6$ (orange), $c = 0.8$ (yellow), $c = 1$ (purple), $c = 1.2$ (green), $c = 1.4$ (cyan).

A decrease of c implies a reduction of the gravity component parallel to the substrate and thus a reduction of the pole thickness, for a given time horizon. The film thinning or thickening moving downstream of the pole is also related to the considered geometry, as the consequence of two competing effects, already shown close to the pole (§ 2.3), where the thickness evolution depends on the normal gravity component multiplied by the local mean curvature $(\mathbf{g} \cdot \mathbf{e}_3)\mathcal{K}$. While at the pole gravity is aligned with the substrate normal, i.e. $\mathbf{g} \cdot \mathbf{e}_3 = 1$, as we move away the normal gravity component $\mathbf{g} \cdot \mathbf{e}_3$ decreases with the zenith owing to the slope increase of the substrate, leading to a first inhomogeneity mechanism. Moving away from the pole, this slope increase leads to a slower decrease of the thickness with time. This explains why, in the case of constant curvature, e.g. spheres or cylinders, the thickness increases moving toward the equator, in agreement with the results of Lee *et al.* (2016) and Balestra *et al.* (2018a). The second mechanism at hand is the evolution of the curvature \mathcal{K} along the zenith direction. Curvature variations induce an accumulation of fluid in regions of lower curvature, characterized by a slower decrease of the thickness with time. Spheroids with small height are characterized by a mean curvature that increases away from the pole, and *vice versa* for spheroids of large height. The former are thus likely to present a decreasing thickness moving downstream, and *vice versa*, as observed in figure 3. As a result, the thickness distribution is a result of the competition between variations of slope and mean curvature, which may induce thinning or thickening of the fluid layer.

Therefore, the transition does not occur when the mean curvature is constant (i.e. $c = 1$), but when there is a balance between the thickness variations due to the change in mean curvature and those induced by slope variations. This value can be obtained by considering the quantity on the right-hand side of (2.9), i.e. $(\mathbf{g} \cdot \mathbf{e}_3)\mathcal{K}$, which, in the vicinity of the pole, reads

$$(\mathbf{g} \cdot \mathbf{e}_3)\mathcal{K} \approx -(2c - c(3c^2 - 2))\vartheta^2 + O(\vartheta^4), \quad (3.7)$$

which is constant for $c = c^*$, i.e. the value that causes the $O(\vartheta^2)$ contribution to vanish. Note that the same transition value can be obtained by evaluating how the quantity $(1/w)\partial_1(wg_t^{(1)})$ perturbs the $O(1)$ solution. The non-monotonic behaviours at large ϑ for $c < c^*$ are related to higher-order terms.

3.2. Spreading problem

Typical coating applications involve the spreading of an initial volume of fluid located close to the top of the considered geometry (Takagi & Huppert 2010). Here, following previous works (Huppert 1982a), we recover some typical relevant quantities such as the position and thickness of the spreading front. An initial volume of fluid V is released on the substrate. We impose the conservation of mass in general coordinates, under the assumption $\delta = 0$ (Roy *et al.* 2002):

$$\int \int_S h(x^{(1)}, x^{(2)}, t) w \, dx^{(1)} \, dx^{(2)} = V, \quad (3.8)$$

where V is the initial volume released on the substrate and S is the region of the substrate, parameterized with $(x^{(1)}, x^{(2)})$, which contains the fluid and varies with time because of the moving front. Far from the contact line, the drainage solution $h(x^{(1)}, x^{(2)}, t)$ can be employed, while capillary effects are relevant only in the close vicinity of the front (Huppert 1982a). For a fixed substrate geometry, w is known, and thus relation (3.8) is an implicit equation with the front position as an unknown. A typical assumption to simplify the analysis is the employment of the large-time drainage solution.

We consider an initial volume of fluid of constant height $h_i = 1$ released at $t = 0$ in the region $0 < \varphi < 2\pi$, $0 < \vartheta < \vartheta_0$. Owing to the invariance along the azimuthal direction, the conservation of the initial fluid volume (3.8) reads

$$\int_0^{\vartheta_F(t)} h(\vartheta, t) w(\vartheta) \, d\vartheta = \int_0^{\vartheta_0} 1 w(\vartheta) \, d\vartheta, \quad (3.9)$$

where $\vartheta_F(t)$ is the front angle; the analytical expression (3.6) for $h(\vartheta, t)$ is employed. Equation (3.9) is numerically solved in Matlab via the built-in function 'fsolve'. Figure 4(a) shows the evolution of the front angle ϑ_F with time, for different values of ϑ_0 and c . An increase in ϑ_0 leads to larger values of ϑ_F , for fixed time. At small times, an increase in c leads to larger ϑ_F ; however, at large times, the opposite behaviour is observed. In figure 4(b) we report the thickness at the front $h_F = h(\vartheta_F(t), t)$, which presents slight variations with c .

We approximate these results by considering an expansion for $\vartheta \ll 1$, by employing equation (3.4a,b) for $t \gg 1$, and $w(\vartheta) = \vartheta + O(\vartheta^2)$. In this case, both the right-hand side and left-hand side of (3.9) can be analytically integrated and an explicit relation for ϑ_F is found, together with an expression of the thickness at the front h_F

$$\sqrt{\frac{3}{4t}} \frac{1}{\sqrt{c}} \frac{\vartheta_F^2}{2} = \frac{\vartheta_0^2}{2} \rightarrow \vartheta_F = \vartheta_0 \left(\frac{4ct}{3} \right)^{1/4}, \quad h_F = \left(\frac{\vartheta_0}{\vartheta_F} \right)^2. \quad (3.10a,b)$$

Note that this expression with $c = 1$ coincides with the solution on a sphere (Takagi & Huppert 2010). These results, reported in the black dashed line in figure 4(a,b), agree well with the implicit equation for small values of ϑ . The velocity of the front $U_F = d\vartheta_F/dt = (c/192)^{1/4} t^{-3/4}$ decreases with time. Therefore, the front slows down as moving downstream toward the equator, for all values of c .

We verify the faithfulness of this approach by comparing it with the numerical results of the complete model (2.4) with parameters $c = 0.6$, $Bo = 500$ and $\delta = 10^{-3}$ (figure 4c). To simulate the spreading on the substrate, we consider a precursor film of size $h_{pr} = 0.005$

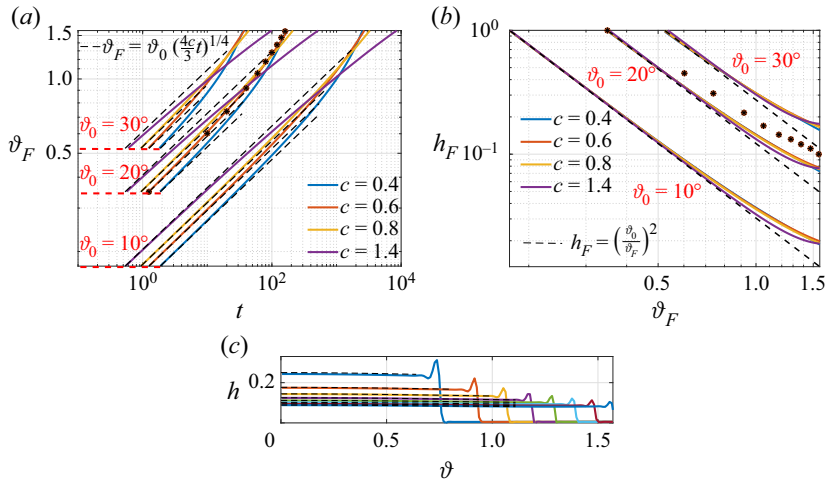


Figure 4. Spreading of an initial volume of fluid on a spheroid. (a) Variation of the front angle ϑ_F with time and (b) of the thickness at the front h_F with ϑ_F , for different values of c (coloured lines) and ϑ_0 (different clusters of curves). The black dashed lines correspond to the analytical approximation of the relation $\vartheta_F(t)$ and $h_F(\vartheta_F)$, while the stars are the values recovered by a numerical simulation of the complete model with $c = 0.6$, $Bo = 500$, $\delta = 10^{-3}$. (c) Numerical thickness distribution obtained from the complete model with $c = 0.6$, $Bo = 500$, $\delta = 10^{-3}$ as a function of ϑ at different times: $t = 20$ (blue), $t = 40$ (orange), $t = 60$ (yellow), $t = 80$ (purple), $t = 100$ (green), $t = 120$ (cyan), $t = 140$ (maroon), $t = 160$ (blue). The black dashed lines denote the corresponding leading-order large-time drainage solution.

(Troian, Wu & Safran 1989b; Kondic & Diez 2002) with the following initial condition (Balestra *et al.* 2019):

$$h(\vartheta, 0) = \frac{h_i - h_{pr}}{2} (1 - \tanh(100(\vartheta - \vartheta_0))) + h_{pr}. \quad (3.11)$$

Figure 4(c) shows the evolution with time of the film thickness, with $\vartheta_0 = 20^\circ$. In the vicinity of the front, a capillary ridge connects the film to the precursor one. Far from the front, the drainage solution approximates well the thin film evolution. In figure 4(a,b), we report also the position and the values of the maximum thickness at the ridge, with a good agreement with the analytical approach.

The spreading velocity decreases with time and is proportional to $c^{1/4}$, in the vicinity of the pole. As c increases, for fixed ϑ_F , the tangential gravity component increases while the area invaded by the fluid does not vary, at leading order ($w \approx \vartheta$), close to the pole. The propagation velocity therefore increases since a faster drainage is observed with increasing c . Nevertheless, at large times, spheroids with smaller c present larger values of ϑ_F . Close to the equator, the tangential gravity component is almost vertical and thus the film velocity is not strongly affected by c . Nevertheless, for fixed equatorial radius, the distance covered for a small increment $d\vartheta_F$ increases with c , at large ϑ_F , therefore implying a reduction of the spreading velocity $d\vartheta_F/dt$.

In this section, we described the competition between the substrate’s slope and curvature in defining the drainage and spreading patterns on an axisymmetric substrate, the spheroid. In the ESM, we report also the case of a paraboloid, which instead always shows a decreasing mean curvature and thus an increasing thickness moving away from the pole. The spheroid analysis was simplified thanks to the absence of odd terms in the asymptotic expansion in ϑ . To better understand the role of the curvature in modifying the drainage, we now consider the torus, a substrate in which the symmetry with respect to ϑ is broken.

4. Non-symmetric drainage and spreading: coating of a torus

4.1. Drainage problem

In this section, we consider the drainage of a thin film flowing on a toroidal substrate of tube radius R and distance dR between the axis of revolution and the centre of the tube (see [figure 5a](#)). The torus is thus generated by the rotation along the azimuthal direction of a circular cross-section whose centre is located at a distance d from the axis of rotation. Non-dimensionalizing the in-plane directions and substrate variables with R , the following parameterization based on the zenith ϑ and the azimuth φ is employed:

$$X(\vartheta, \varphi) = ((d + \sin \vartheta) \cos \varphi, (d + \sin \vartheta) \sin \varphi, \cos \vartheta). \quad (4.1)$$

The position along the cylinder, at each azimuthal circular cross-section, is defined through the zenith ϑ . Two limiting cases are identified; the first one occurs for $d \rightarrow \infty$, which leads to the cylindrical case, reported in the ESM. The second case occurs for $d = 1$, in which the points at $\vartheta = -90^\circ$ are in contact, leading to the so-called horn torus. The gravity term $g_t^{\{1\}}$ and w read

$$g_t^{\{1\}}(\vartheta) = \sin(\vartheta), \quad w(\vartheta) = d + \sin(\vartheta). \quad (4.2a,b)$$

The same procedure employed for the drainage solution of the spheroidal case is adopted. However, in this case we cannot *a priori* neglect the odd terms in the asymptotic expansion, i.e. $h(\vartheta, t) = H_0(t) + \vartheta H_1(t) + \vartheta^2 H_2(t) \dots$. The resulting problems, at different orders in ϑ , are reported in [Appendix B](#). For the sake of brevity, the large-time solution at $O(\vartheta^4)$ reads

$$h = \sqrt{\frac{3}{2t}} \left(\frac{19\,377\vartheta^4}{176\,000d^4} - \frac{1409\vartheta^3}{11\,000d^3} - \frac{7477\vartheta^4}{147\,840d^2} + \frac{31\vartheta^2}{200d^2} + \frac{91\vartheta^3}{2640d} - \frac{\vartheta}{5d} + \frac{43\vartheta^4}{10\,752} + \frac{\vartheta^2}{16} + 1 \right) + O(\vartheta^5) + O\left(\frac{1}{t^{3/2}}\right). \quad (4.3)$$

The cylinder thickness distribution is recovered for $d \rightarrow \infty$ (Balestra *et al.* 2018a). The $O(1)$ solution is analogous to the cylinder case for any value of d . The drainage problem is numerically solved in the domain $-\pi/2 < \vartheta < \pi/2$. Numerical convergence is achieved with $\Delta\vartheta = 0.5^\circ$. [Figure 5](#) shows a comparison between the numerical and large-time analytical solutions of the drainage problem, for different values of d in the range $-\pi/2 < \vartheta < \pi/2$. The distribution is not symmetric with respect to $\vartheta = 0$. In particular, the thickness is larger for negative values of ϑ , i.e. on the inner side of the torus, while for $\vartheta > 0$ the thickness is almost constant. These differences are enhanced as d decreases. The numerical solution compares well with the analytical one at $O(\vartheta^4)$ while, at $O(\vartheta^2)$, the agreement is good only in the vicinity of the top.

At the top ($\vartheta = 0$), $\mathcal{K} = -1$ and therefore the film drains as in the cylinder case, locally. The different thickness distributions in the two sides of the circular cross-section of the torus result from the non-symmetric drainage with respect to ϑ . While the slope is symmetric with respect to ϑ , the mean curvature decreases on the inner part and decreases on the outer part. Following the discussion of [§ 3.1](#), a decreasing (respectively increasing) curvature induces an increasing (respectively decreasing) thickness. Therefore, much larger thicknesses are attained on the inner part than on the outer one, where the thickness slightly decreases, in the vicinity of the top. The slight increase on the outer part observed at large ϑ is due to the saturation of the mean curvature value, which remains almost constant, while the substrate's slope increases. From a quantitative point of view,

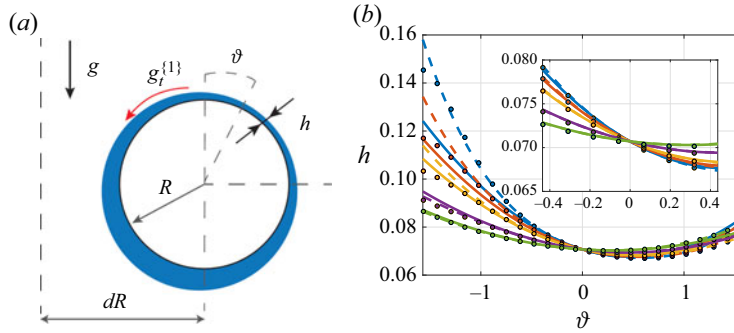


Figure 5. (a) Sketch of the axisymmetric flow configuration for the coating of a torus. (b) Drainage solution on a torus at $t = 300$, numerical (coloured dots) and analytical solutions at order $O(\vartheta^2)$ (solid lines) and $O(\vartheta^4)$ (dashed lines), for $d = 1.1$ (blue), $d = 1.25$ (orange), $d = 1.5$ (yellow), $d = 2.5$ (purple), $d = 5$ (green).

we consider the product between the normal component of gravity and the mean curvature

$$(\mathbf{g} \cdot \mathbf{e}_3) \mathcal{K} \approx - \left(\left(-\frac{1}{a^2} - \frac{1}{2} \right) \vartheta^2 + \frac{\vartheta}{a} + 1 \right), \quad (4.4)$$

which shows a decrease on the inner part, thus highlighting an accumulation of fluid downstream, and *vice versa*. The same result could be obtained by considering how the flux perturbs the $O(1)$ solution.

4.2. Spreading problem

We now present the results for the spreading of a volume of fluid on a torus. We consider an initial volume of fluid of thickness $h = 1$ in the region $-\vartheta_0 < \vartheta < \vartheta_0$. The breaking of symmetry with respect to $\vartheta = 0$ results in two different spreading fronts for $\vartheta < 0$ (inner side) and $\vartheta > 0$ (outer side). However, at $\vartheta = 0$, the drainage gravity component is exactly zero, i.e. $q^{\{1\}} = h^3 g_t^{\{1\}} h^3 = 0$. Therefore, the total volume on each side of the torus is conserved since there is no flux at $\vartheta = 0$. Note that, when hydrostatic or capillary effects are considered, the flux is not exactly zero at the top. A preliminary analysis showed that appreciable variations of the mass on the two sides (of the order of 2%) are observed for $Bo = 250$ and $\delta = 0.1$, when either pure capillary or pure hydrostatic effects are considered, in addition to drainage. For larger values of Bo or smaller values of δ , these differences rapidly decrease. In the limit $Bo \rightarrow \infty$ and $\delta = 0$ (i.e. the considered drainage problem), a zero flux at the top of the torus is numerically observed.

The conservation of mass for the two regions reads

$$\int_0^{\vartheta_F^O(t)} h(\vartheta, t) w(\vartheta) \, d\vartheta = \int_0^{\vartheta_0} w(\vartheta) \, d\vartheta, \quad \int_{-\vartheta_F^I(t)}^0 h(\vartheta, t) w(\vartheta) \, d\vartheta = \int_{-\vartheta_0}^0 w(\vartheta) \, d\vartheta, \quad (4.5a,b)$$

where $\vartheta_F^O(t)$ and $\vartheta_F^I(t)$ are the front angle on the outer and inner part, respectively, $w(\vartheta) = d + \sin(\vartheta)$ and $h(\vartheta, t)$ is given by (4.3). Note that the two integrals on the right-hand side do not assume the same value, since $w(\vartheta)$ is not symmetric with respect to $\vartheta = 0$. Equations (4.5a,b) are implicit integrals that are solved in Matlab through the built-in function ‘fsolve’. A first analytical approximation is found by taking the $O(1)$

approximation, leading to

$$\frac{\vartheta_F^O}{\vartheta_0} = \frac{\vartheta_F^I}{\vartheta_0} = \sqrt{\frac{2t}{3}}, \tag{4.6}$$

i.e. the solution of $O(1)$ does not depend on d and is analogous to the spreading on a cylinder (Balestra *et al.* 2018a). The thickness at the front thus reads $h_F = \vartheta_0/\vartheta_F$. A better approximation that includes the curvature of the torus can be obtained by considering the $O(\vartheta)$ approximation of the integrand

$$\left. \begin{aligned} & \int_0^{\vartheta_F^O(t)} \sqrt{\frac{3}{2t}} \left(\frac{4}{5}\vartheta + d \right) d\vartheta = \int_0^{\vartheta_0} (d + \vartheta) d\vartheta \\ & \rightarrow \left(\vartheta_F^O \right)^2 + \frac{5d}{2}\vartheta_F^O - \left(\frac{5}{2}(d\vartheta_0 + \vartheta_0^2/2) \right) \sqrt{\frac{2t}{3}} = 0, \\ & \rightarrow \vartheta_F^O(t) = \frac{1}{2} \left(-\frac{5d}{2} + \sqrt{\frac{25d^2}{4} + 4(d\vartheta_0 + \vartheta_0^2/2)\frac{5}{2}\sqrt{\frac{2t}{3}}} \right), \end{aligned} \right\} \tag{4.7}$$

$$\left. \begin{aligned} & \int_{-\vartheta_F^I(t)}^0 \sqrt{\frac{3}{2t}} \left(\frac{4}{5}\vartheta + d \right) d\vartheta = \int_{-\vartheta_0}^0 (d + \vartheta) d\vartheta \\ & \rightarrow \left(\vartheta_F^I \right)^2 - \frac{5d}{2}\vartheta_F^I + \left(\frac{5}{2}(d\vartheta_0 - \vartheta_0^2/2) \right) \sqrt{\frac{2t}{3}} = 0, \\ & \rightarrow \vartheta_F^I(t) = \frac{1}{2} \left(\frac{5d}{2} - \sqrt{\frac{25d^2}{4} - 4(d\vartheta_0 - \vartheta_0^2/2)\frac{5}{2}\sqrt{\frac{2t}{3}}} \right). \end{aligned} \right\} \tag{4.8}$$

Figure 6(a,b) shows the behaviours of ϑ_F^O , ϑ_F^I and the front thicknesses h_F^O and h_F^I on the inner and outer sides of the torus, respectively, for different values of d and ϑ_0 . As concerns panel (a), for a fixed time, the front angle on the inner side is always larger than the one on the outer side. An increase of d leads to a decrease (respectively increase) of ϑ_F on the inner (respectively outer) side. The front thickness does not strongly depend on d , even if some differences can be appreciated on the inner side, for large values of ϑ_F^O . The $O(1)$ approximation gives a reasonable agreement in the prediction of the front angle and thickness. In particular, it appears to be the lower (respectively upper) limit for the inner (respectively outer) sides, as d increases. The order $O(\vartheta)$ approximations follow well the implicit relations (4.5a,b). We compare these analytical results with a numerical simulation of the complete model (2.4) with parameters $d = 1.25$, $Bo = 500$, $\delta = 10^{-3}$, $h_{pr} = 0.005$, initial condition

$$h(\vartheta, 0) = \frac{h_i - h_{pr}}{2} (1 - \tanh(100(\vartheta - \vartheta_0))) + h_{pr}, \quad \text{for } \vartheta > 0, \tag{4.9}$$

$$h(\vartheta, 0) = \frac{h_i - h_{pr}}{2} (1 - \tanh(100(-\vartheta - \vartheta_0))) + h_{pr}, \quad \text{for } \vartheta < 0, \tag{4.10}$$

and $\vartheta_0 = 10^\circ$ (see figure 6c). The agreement between the numerical front angle, given by the maximum thickness location, and the theoretical one is very good, and also the maximum thickness well follows the front thickness predicted by the theory.

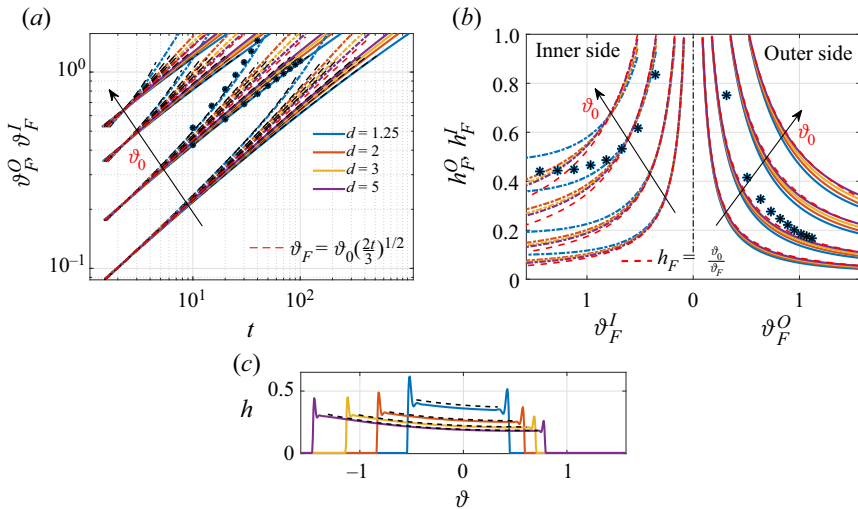


Figure 6. Spreading of an initial volume of fluid on a torus. (a) Variation of the front angle ϑ_F with time and (b) of the thickness at the front h_F with ϑ_F , for different values of the initial angle ϑ_0 and d . The solid and dot-dashed lines denote the values of ϑ_F and h_F on the outer and inner sides, respectively. The black and red dashed lines correspond to the $O(1)$ and $O(\vartheta)$ analytical approximations of the relation $\vartheta_F(t)$ and $h_F(\vartheta_F)$, respectively, while the stars are the values recovered by a numerical simulation of the complete model with $d = 1.25$, $Bo = 500$, $\delta = 10^{-3}$, precursor film thickness $h_{pr} = 0.005$. (c) Numerical thickness distribution obtained from the complete model with $d = 1.25$, $Bo = 500$, $\delta = 10^{-3}$ as a function of ϑ at different times: $t = 10$ (blue), $t = 20$ (orange), $t = 30$ (yellow), $t = 40$ (purple). The black dashed lines denote the corresponding large-time drainage solutions.

In analogy with the drainage solution, the faster spreading attained on the inner region is related to the substrate geometry. For a fixed angular distance from the top, the area covered by the spreading fluid is larger on the outer region than on the inner one. Therefore, for a fixed time, the fluid spreads faster on the inner region, reaching larger values of ϑ_F than on the outer region. Interestingly, the solution at $O(1)$ does not capture the symmetry breaking, since, at the top, a torus locally coincides with a cylinder. Nevertheless, the $O(\vartheta)$ approximation already captures the asymmetry of the substrate.

The torus case shows non-symmetric drainage and spreading along the zenith direction. In the following, we present how these analyses can be extended to non-axisymmetric substrates which are characterized by a three-dimensional, non-uniform along the azimuthal direction, drainage. We chose as a testing ground an ellipsoid with three different axes.

5. Three-dimensional drainage and spreading: coating of an ellipsoid

5.1. Numerical drainage solution

In this section, we study the coating of an ellipsoidal substrate of horizontal semiaxes aR , bR and vertical semiaxis R (see figure 1); gravity is pointing downward. In non-dimensional form, the following parameterization holds:

$$X(\vartheta, \varphi) = (a \sin \vartheta \cos \varphi, b \sin \vartheta \sin \varphi, \cos \vartheta). \tag{5.1}$$

We identify different limiting cases, depending on the values of a and b . If $a = b = 1$, we recover the spherical case; if $a = b \neq 1$ the resulting substrate is an axisymmetric ellipsoid of unitary height and equatorial radius $a = b$, whose results can be recovered

from those of § 3.1. Note that the time scale is different since the in-plane directions and substrate variables are non-dimensionalized with the height and not with the equatorial radius, in the present section. When $a \neq b$ the axisymmetry is broken since the two axes at the equator are different. In the following, we assume that $b \geq a$ and consider the range $0.4 < a, b < 2$. Note that the solutions for $a > b$ can be recovered by simply translating of $\varphi = 90^\circ$ the solution for $b \geq a$ (obtained by swapping the desired values of a and b).

The metric components vary along the φ direction; in particular, the metric tensor is not diagonal (see the ESM). The local coordinates system defined by the parameterization is thus non-orthogonal and a second gravity component $g_t^{[2]}(\vartheta, \varphi)$, appears. The square root of the determinant of the metric and the gravity terms now read

$$w(\vartheta, \varphi) = \sqrt{\sin^4(\vartheta) (a^2 \sin^2(\varphi) + b^2 \cos^2(\varphi)) + a^2 b^2 \sin^2(\vartheta) \cos^2(\vartheta)}, \quad (5.2)$$

$$g_t^{[1]}(\vartheta, \varphi) = \frac{\sin(\vartheta) (a^2 \sin^2(\varphi) + b^2 \cos^2(\varphi))}{\sin^2(\vartheta) (a^2 \sin^2(\varphi) + b^2 \cos^2(\varphi)) + a^2 b^2 \cos^2(\vartheta)}, \quad (5.3)$$

$$g_t^{[2]}(\vartheta, \varphi) = \frac{\sin(\varphi) \cos(\varphi) (a^2 \cos(\vartheta) - b^2 \sin(\vartheta))}{a^2 b^2 \cos^2(\vartheta) \cos^2(\varphi) + a^2 b^2 \cos^2(\vartheta) \sin^2(\varphi) + a^2 \sin^2(\vartheta) \sin^2(\varphi) + b^2 \sin^2(\vartheta) \cos^2(\varphi)}. \quad (5.4)$$

We solve (2.6) by imposing periodic boundary conditions in $0 < \varphi < 2\pi$ and the initial condition $h(\vartheta, \varphi, 0) = 1$. Numerical convergence is achieved with a characteristic mesh size of 0.9° . Figures 7 and 8 respectively show the resulting film distributions and a section at $\vartheta = \pi/4$ for different values of a and b , at $t = 100$. We first increase the value of b , with $a = 1$. For $b = 1.2$ (panel (a)), the thickness presents modulations along the azimuthal direction, with a maximum thickness localized at $\varphi = k\pi$ ($k = 0, 1, 2$), i.e. along the direction of the smaller axis a . These modulations are enhanced as b increases (panel (b)), with larger values of the attained thickness. Two regions of low thickness are localized at $\varphi = \pi/2 + k\pi$, along the larger axis b . The same trends are observed further increasing b (panel (c)). When $b = 1$ and a decreases (panel (d)), the thickness also presents modulations along the azimuthal direction, but the thickness always increases moving downstream. The thickness decreases as a decreases. Similar patterns are also obtained when small values of a and large values of b are considered. The numerical solution of (2.6) shows the presence of modulations of the thickness along the azimuthal direction. According to § 3.1, spheroids with small (respectively large) height were characterized by a decrease (respectively increase) of the thickness. We can extend these considerations to an ellipsoid by considering the drainage along the principal directions defined by (x, y) , see figure 1(c). Since the drainage component along the azimuthal direction is identically zero along the two principal semi-axes, the flow locally behaves like the spheroidal case of § 3.1. Therefore, we expect to follow these trends along the two semi-axes, depending on a and b . In the axisymmetric case, the thickness increases downstream for height–radius ratios larger than 0.74, which corresponds to $a, b \lesssim 1.35$. Therefore, when $a, b \lesssim 1.35$ we always observe an increase of the thickness with ϑ , as observed in figure 9(a–c) (see also figure 3 for the cases with $c > c^*$). However, the thickness presents clear modulations owing to the non-uniform drainage when $a \neq b$. Similarly, when $a, b \gtrsim 1.35$ one expects a decrease of the thickness followed by a slight increase at large ϑ , with modulations if $a \neq b$, as shown in figure 9(d–g). The intermediate situation occurs when $a \lesssim 1.35$ and $b \gtrsim 1.35$, characterized by an increase of the thickness along the x direction and a decrease along the y direction, as observed in figure 7(b,c,g).

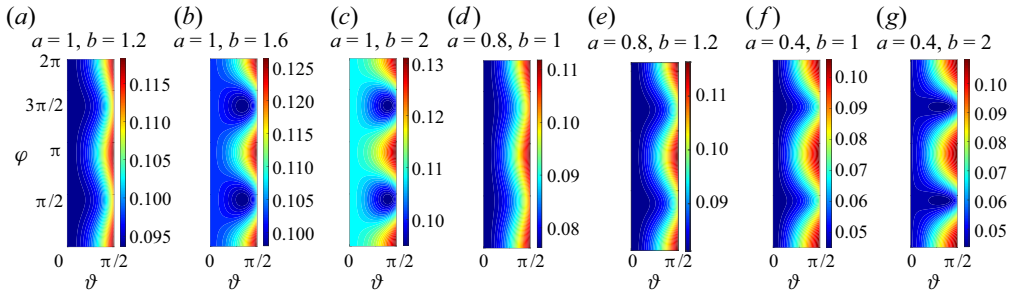


Figure 7. Numerical solution of (2.6) at $t = 100$ as a function of (ϑ, φ) , for different values of the semiaxes a and b , with $a \leq 1$ and $b \geq 1$.

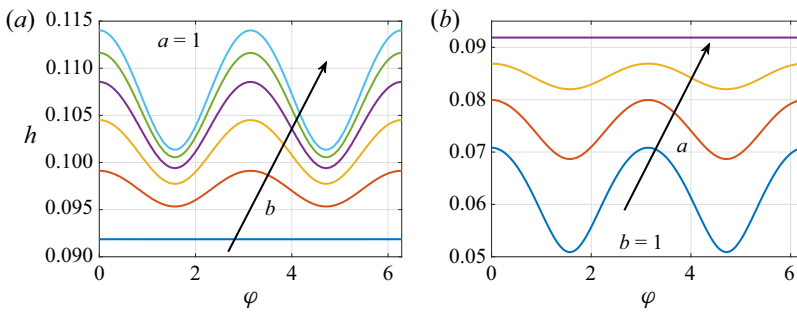


Figure 8. Numerical solution of (2.6) at $t = 100$ and $\vartheta = \pi/4$ as a function of (φ) : (a) $a = 1$ and $b = 1$ (blue), $b = 1.2$ (orange), $b = 1.4$ (yellow), $b = 1.6$ (purple), $b = 1.8$ (green), $b = 2$ (cyan); (b) $b = 1$ and $a = 0.4$ (blue), $a = 0.6$ (orange), $a = 0.8$ (yellow), $a = 1$ (purple).

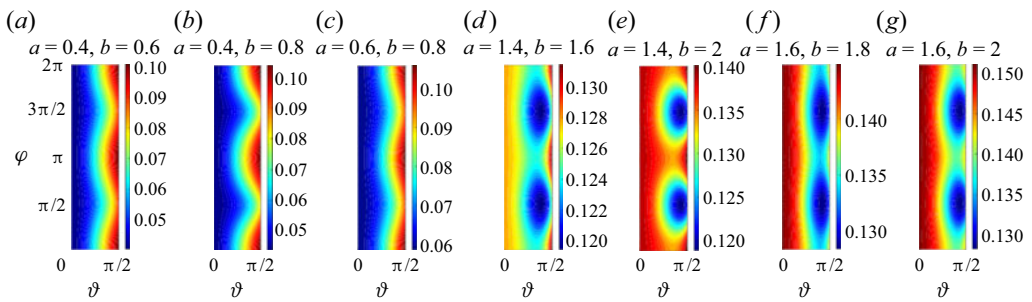


Figure 9. Numerical solution of (2.6) at $t = 100$ as a function of (ϑ, φ) , for different values of the semiaxes a and b , with $a, b < 1$ and $a, b > 1$.

The modulations of the thickness distribution are related to the variation of drainage with the azimuth. In the vicinity of the minor semiaxis, the tangential gravity component along the zenith is larger than close to the major semiaxis. Higher velocities are thus attained along the minor semiaxis, displacing more fluid downstream than along the major semiaxis. This process induces transport of fluid from progressively farther and farther regions and thus a secondary flow from the major semiaxis (associated with low velocities) to the minor semiaxis (associated with large velocities). In the light of this discussion, one may wonder if these patterns persist with time or merely represent a snapshot of a more

intricate evolution. In the following, we also aim at clarifying this aspect by deriving an analytical solution for the drainage problem.

5.2. Analytical drainage solution

In this section, we derive an analytical drainage solution and compare it with the numerical results of the previous section. In analogy with § 3.1, we perform an asymptotic expansion in powers of ϑ , with $\vartheta \ll 1$. The solution at order $O(1)$ does not depend on φ since the solution at the pole has to be unique. We thus consider the following expansion, in which the odd terms have been removed because of symmetry:

$$h(\vartheta, \varphi, t) = H_0(t) + \vartheta^2 H_2(\varphi, t) + \vartheta^4 H_4(\varphi, t) + \vartheta^6 H_6(\varphi, t) + \dots \quad (5.5)$$

We expand (2.6) at various orders in ϑ . At order $O(1)$, one obtains the following ordinary differential equation (ODE):

$$\frac{1}{3} \left(\frac{1}{a^2} + \frac{1}{b^2} \right) H_0(t)^3 + H_0'(t) = 0 \rightarrow H_0(t) = \frac{1}{\sqrt{\frac{2}{3}t \left(\frac{1}{a^2} + \frac{1}{b^2} \right) + 1}} = \frac{1}{\sqrt{\alpha t + 1}}, \quad (5.6)$$

where $\alpha = \frac{2}{3}(1/a^2 + 1/b^2)$. Also in this case, the $O(1)$ solution reduces to $(3/(2\mathcal{K}_p t))^{1/2}$ at late time, with $\mathcal{K}_p = (1/a^2 + 1/b^2)$. The equation at order $O(\vartheta^2)$ reads

$$\begin{aligned} & \frac{\partial H_2(\varphi, t)}{\partial t} \\ &= \frac{H_0(t)^2((b^2 - a^2) \sin(2\varphi) \frac{\partial H_2}{\partial \varphi} + 2H_2((a^2 - b^2) \cos(2\varphi) - 2(a^2 + b^2)))}{2a^2b^2} \\ &+ \frac{H_0(t)^3((a^4(b^2 - 2) - a^2b^4 + 2b^4) \cos(2\varphi) + 2(a^4(-(b^2 - 1)) + a^2(b^2 - b^4) + b^4))}{6a^4b^4}, \quad (5.7) \end{aligned}$$

which is a parabolic partial differential equation (PDE) in $H_2(\varphi, t)$. We numerically solve (5.7) with initial condition $H_2(\varphi, 0) = 0$. The periodic boundary conditions at $\varphi = [0, 2\pi]$ are automatically imposed thanks to a Fourier spectral collocation method implemented in Matlab. The time stepping is performed by employing the built-in function ‘ode23t’, with a tolerance of 10^{-6} . Numerical convergence is achieved with 100 collocation points.

Figure 10(a) shows the spatio-temporal evolution of the second-order solution $H_2(\varphi, t)$, for $a = 0.5$ and $b = 1.5$. An initial growth in absolute value until $t \approx 0.3$ is followed by a slow decay at large times. In figure 10(b) we report the H_2 profiles rescaled with H_0 , at different times in the slow-decay regime. The second-order solution H_2 is π -periodic and the maximum is attained at $\varphi = k\pi$, i.e. along the smaller axis of the ellipsoid. At $\varphi = k\pi/2$, i.e. along the larger axis of the ellipsoid, the correction reaches much smaller values. As time increases, the profiles collapse on a single curve, suggesting that a large-time solution characterized by a separation of variables is possible, i.e. $H_2(\varphi, t) = H_0(t)H_2^*(\varphi)$. We introduce this decomposition in (5.7). Exploiting (5.6), the

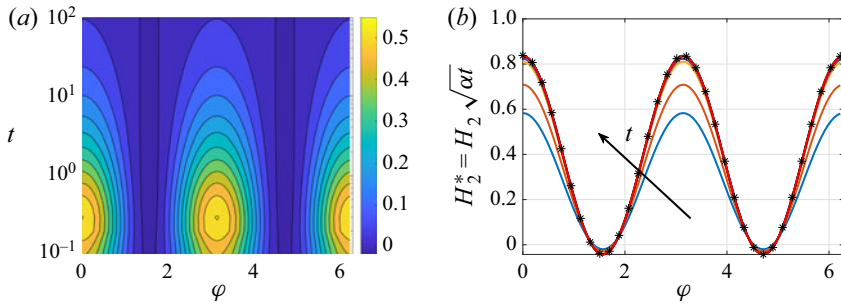


Figure 10. Drainage on an ellipsoid with $a = 0.5$ and $b = 1.5$. (a) Spatio-temporal evolution of H_2 : iso-contours of H_2 in the (φ, t) plane. (b) Second-order correction $H_2^* = H_2/H_0 \approx H_2\sqrt{\alpha t}$ as a function of φ at different times: $t = 0.4$ (blue), $t = 1$ (orange), $t = 5$ (yellow), $t = 10$ (purple), $t = 30$ (green), $t = 50$ (cyan), $t = 70$ (maroon), $t = 90$ (black), $t = 100$ (red). The black stars denote the late-time analytical solution for H_2^* from (5.9).

temporal dependence disappears and the following ODE for $H_2^*(\varphi)$ is obtained:

$$\begin{aligned}
 & -a^4b^2 \cos(2\varphi) + 2a^4b^2 + 2a^4 \cos(2\varphi) - 2a^4 + a^2b^4 \cos(2\varphi) + 2a^2b^4 \\
 & + 3a^2b^2(a^2 - b^2) \sin(2\varphi)H_2'(\varphi) - 2a^2b^2H_2^*(\varphi)(3(a^2 - b^2) \cos(2\varphi) - 5(a^2 + b^2)) \\
 & - 2a^2b^2 - 2b^4 \cos(2\varphi) - 2b^4 = 0,
 \end{aligned} \tag{5.8}$$

whose solution reads

$$\begin{aligned}
 H_2^*(\varphi) &= C_1 \sin(2\varphi) \sin^{-5(a^2+b^2)/3(a^2-b^2)}(\varphi) \cos^{5(a^2+b^2)/3(a^2-b^2)}(\varphi) \\
 & - \frac{1}{8a^2b^2(4a^2 + b^2)(a^2 + 4b^2)} (a^6(7b^2 - 4) + 26a^4(b^4 - b^2) \\
 & + a^2b^4(7b^2 - 26) + (a^2 - b^2)(a^4(b^2 + 4) + a^2b^2(b^2 + 14) + 4b^4) \\
 & \times \cos(2\varphi) - 4b^6),
 \end{aligned} \tag{5.9}$$

where C_1 is a constant to be determined. However, it is observed that $C_1 \neq 0$ implies an unbounded behaviour. Therefore, we impose $C_1 = 0$ to prevent non-physical solutions. The analytical result for H_2^* is reported in figure 10(b), with an excellent agreement with the numerical solution. We then investigate the effect of a and b by considering different cases at $t = 100$, reported in figure 11. An increase of b for fixed $a = 0.5$ (panel (a)) leads to a decrease of H_2^* in the region $\varphi = k\pi/2$, while an increase in a for fixed $b = 1.5$ (panel (b)) shows an overall decrease of H_2^* . Also for these cases, an excellent agreement with the analytical solution is observed. At $O(\vartheta^2)$, the large-time analytical solution can be written in compact form as

$$h \approx H_0(t)(1 + (f(a, b) + g(a, b) \cos(2\varphi))\vartheta^2). \tag{5.10}$$

The modulations observed in the numerical simulations of the previous section are captured by the $O(\vartheta^2)$ term, which is a π -periodic function of the azimuth. These modulations are present as long as $g(a, b) = (a^2 - b^2)(a^4(b^2 + 4) + a^2b^2(b^2 + 14) + 4b^4) \neq 0$. The only case in which modulations are absent occurs when $g(a, b) = 0$ and thus $a = b$, i.e. the spheroidal case. In the latter case, the solution reads $H_2^* = \frac{1}{10}(3/b^2 - 2)$ and is formally analogous to the second-order solution of the spheroid with $c = 1/b$ (see § 3.1).

Gravity-driven coatings on curved substrates

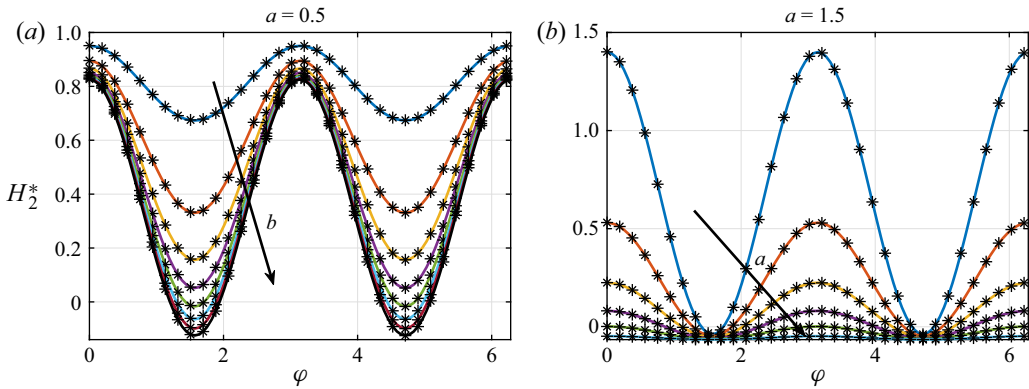


Figure 11. (a) Second-order correction $H_2^* = H_2/H_0 \approx H_2\sqrt{at}$ as a function of φ at $t = 100$, for $a = 0.5$ and increasing b : $b = 0.6$ (blue), $b = 0.8$ (orange), $b = 1$ (yellow), $b = 1.2$ (purple), $b = 1.4$ (green), $b = 1.6$ (cyan), $b = 1.8$ (maroon), $b = 2$ (black); (b) H_2^* as a function of φ at $t = 100$, for $b = 1.5$ and increasing a : $a = 0.4$ (blue), $a = 0.6$ (orange), $a = 0.8$ (yellow), $a = 1$ (purple), $a = 1.2$ (green), $a = 1.4$ (cyan). The black stars denote the late-time analytical solution for H_2^* from (5.9).

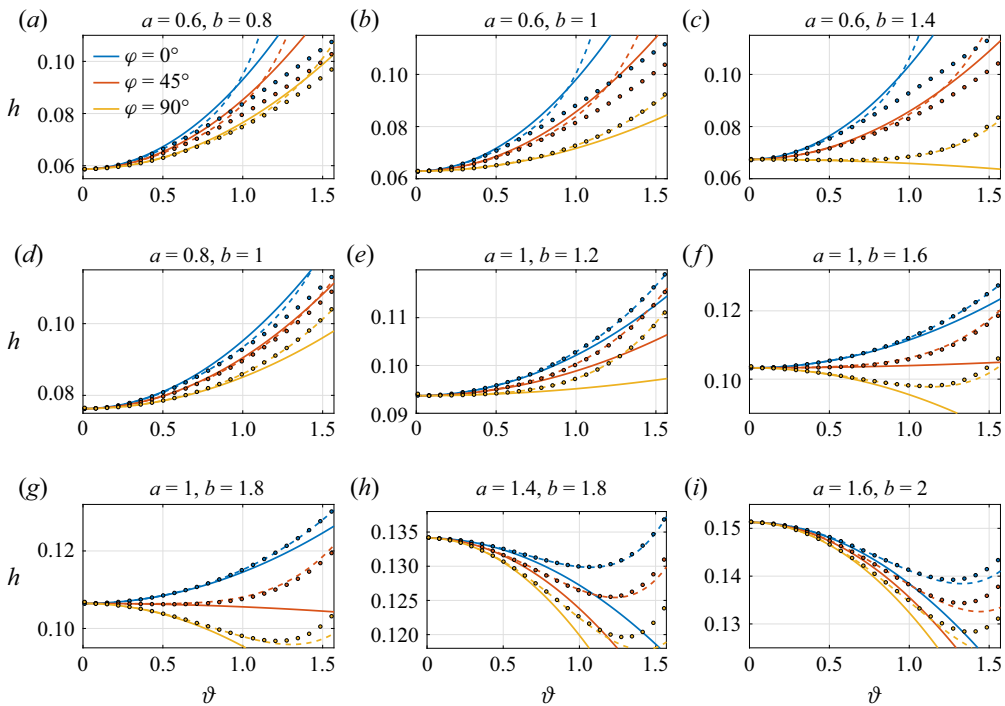


Figure 12. Comparison at three different azimuthal sections between the numerical (coloured dots) and the quasi-analytical solution for an ellipsoid at $O(\vartheta^2)$ (solid lines) and $O(\vartheta^6)$ (dashed lines) at $t = 100$, for different values of a and b .

The faithfulness of the analytical solution is verified against the numerical simulations of § 5.1 in figure 12. For the comparison, we consider the solution at orders $O(\vartheta^2)$ and $O(\vartheta^6)$. The higher-order problems, together with their solutions H_4 and H_6 , are reported in Appendix C. The same large-time behaviour is observed. In general, the analytical

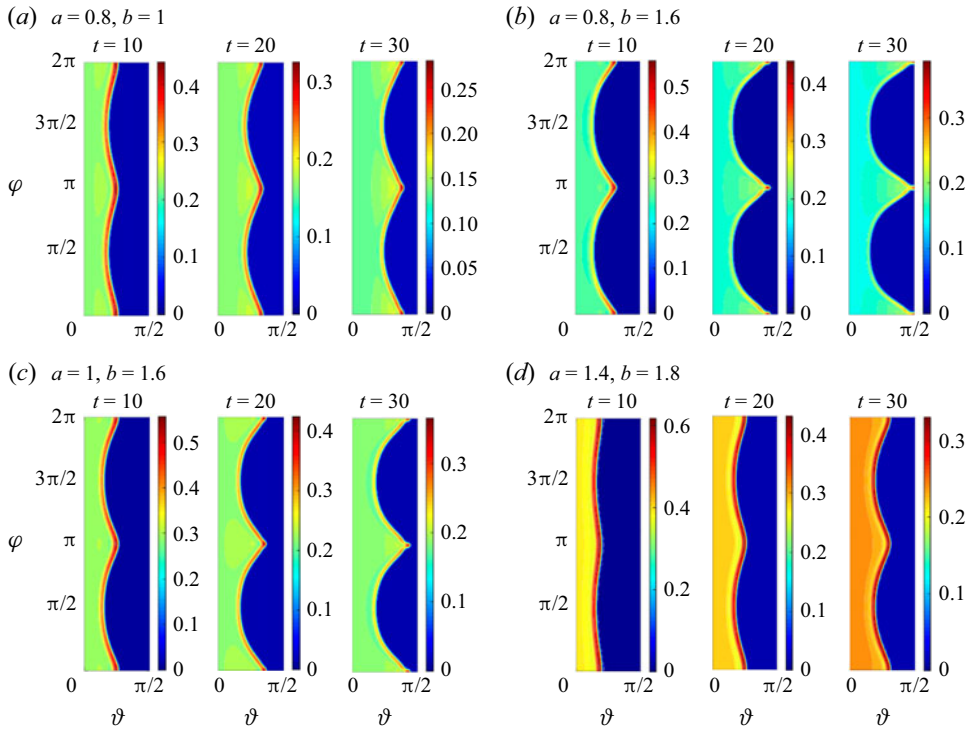


Figure 13. Iso-contours of the numerical solution for the spreading of (2.4), at different times, for an ellipsoid and $Bo = 100$, $\delta = 10^{-2}$, precursor film $h_{pr} = 0.02$ and $\vartheta_0 = 20^\circ$; (a) $a = 0.8$, $b = 1$, (b) $a = 0.8$, $b = 1.6$, (c) $a = 1$, $b = 1.6$, (d) $a = 1.4$, $b = 1.8$.

solutions at $O(\vartheta^6)$ compare well with the numerical ones, while those at $O(\vartheta^2)$ are accurate only in the vicinity of the pole. The analytical solution at $O(\vartheta^6)$ deviates from the numerical one for $a < 0.8$. The agreement for $a > 0.8$ is satisfactory for any value of b .

In this section, we derived an analytical approximation for the drainage problem. The problem was solved by employing an asymptotic expansion in a first stage, followed by a separation of variables at each order of the expansion. The final structure of the analytical approximation (5.10) is characterized by a time dependence separated by the spatial one, similarly to the previous cases. Nevertheless, the power-series expansion presents terms that depend on the azimuth. The simple form of (5.10) captures well the π -periodicity of the drainage solution, induced by the differences in drainage along the minor and major axes. In the spreading problem, these modulations may play a crucial role.

5.3. Spreading problem

In this section, we consider the spreading of an initial volume of fluid of height $h_i = 1$ contained in the region $0 < \vartheta < \vartheta_0$, $0 < \varphi < 2\pi$. Figure 13 shows the evolution of the film thickness with time, for different values of a and b , obtained employing the complete model (2.4) with initial condition formally analogous to (3.11), i.e. invariant along the azimuthal direction. For $t = 10$, the maximum thickness position, at which the front is located, is modulated along the azimuthal direction. This modulation accentuates with time and a region of large thickness forms at $\varphi = k\pi$ (along the shorter axis) while the

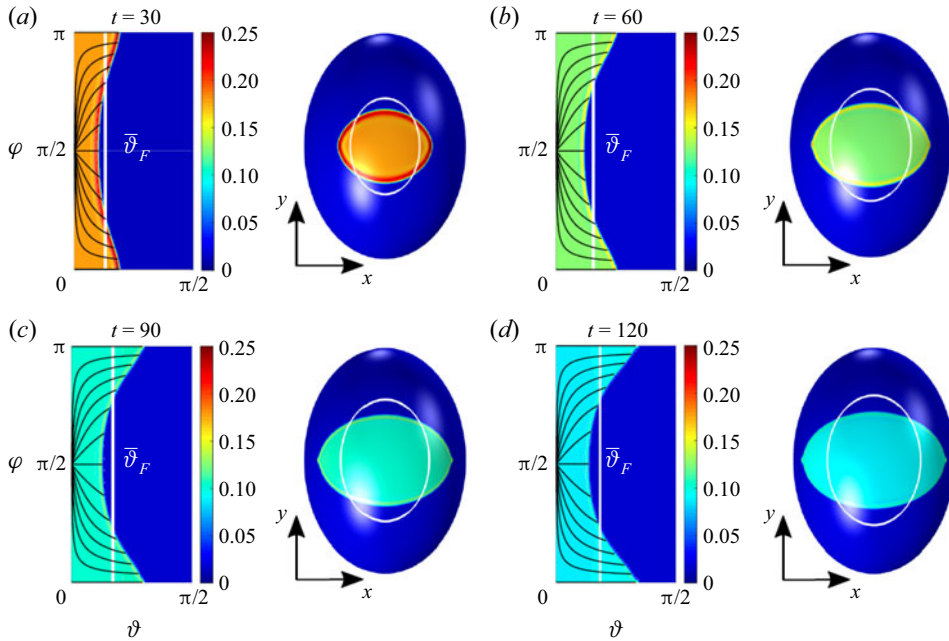


Figure 14. Iso-contours of the numerical spreading solution at different times of (2.4) for an ellipsoid with $a = 1$, $b = 1.4$, $Bo = 1000$, $\delta = 10^{-2}$, precursor film $h_{pr} = 0.02$ and $\vartheta_0 = 10^\circ$. The black solid lines denote the streamlines of the volume flux per unit length q and the white line the average front $\bar{\vartheta}_F$.

thickness is much lower at $\varphi = k\pi/2$. Therefore, the front presents two peaks of large thickness aligned along the shorter axis. This effect is enhanced when larger (respectively lower) values of b (respectively a) are considered.

In figure 14, we report a zoom in the region $0 < \varphi < \pi$ for one simulation of the complete model (2.4) with $Bo = 1000$ and $\delta = 10^{-2}$, together with a three-dimensional rendering of the spreading on the ellipsoid, viewed from the top. The black lines denote the streamlines of the flux $q = q^{\{1\}}e_1 + q^{\{2\}}e_2$. The flux streamlines are almost parallel to the azimuthal direction at low values of ϑ , then bend and align along the zenith direction as ϑ increases. An exception to this behaviour is observed at $\varphi = 0, \pi/2$, in which the flow streamlines are always parallel to the zenith direction. The three-dimensional rendering highlights the formation of two, finger-like, front peaks of large thickness along the shorter axis, while the fluid slowly spreads along the larger axis.

A scaling law for the spreading front and thickness is obtained by neglecting the modulations of the front, and assuming a constant average value along the azimuth, i.e. $\bar{\vartheta}_F = 1/(2\pi) \int_0^{2\pi} \vartheta_F(\varphi, t) d\varphi$. The conservation of volume reads

$$\int_0^{2\pi} \int_0^{\bar{\vartheta}_F(t)} h(\vartheta, \varphi, t) w(\vartheta) d\vartheta d\varphi = \int_0^{2\pi} \int_0^{\vartheta_0} w(\vartheta) d\vartheta d\varphi, \quad (5.11)$$

where $h = H_0(t) + \vartheta^2 H_2(\varphi, t) + \vartheta^4 H_4(\varphi, t) + \vartheta^6 H_6(\varphi, t)$ is the asymptotic solution obtained in the previous section, and w is given by (5.2). Also in this case, an analytical approximation is found by employing the large-time $O(\vartheta)$ approximation (5.6), with $w = ab\vartheta + O(\vartheta^2)$, leading to the following expressions for the average front position and

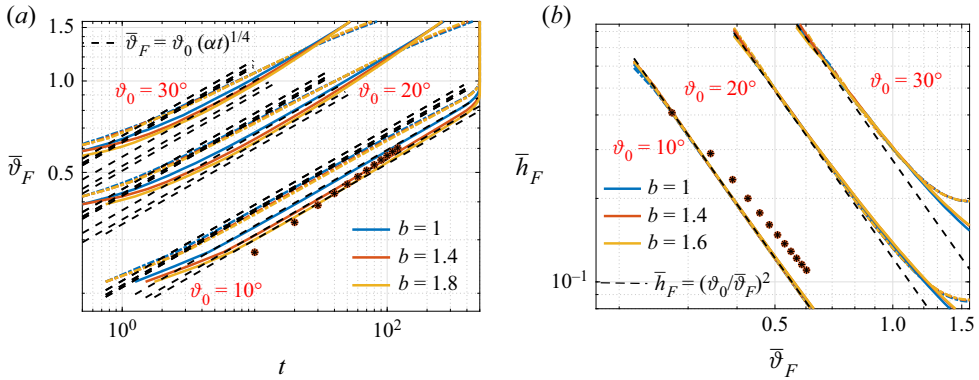


Figure 15. Spreading of an initial volume of fluid on an ellipsoid. (a) Variation of the average front angle $\bar{\vartheta}_F$ with time and (b) of the average thickness at the front \bar{h}_F with $\bar{\vartheta}_F$, for $a = 0.6$ (dash-dotted lines), $a = 1$ (solid lines) and different values of the initial angle ϑ_0 and b . The black dashed lines correspond to the analytical approximation of the relation $\bar{\vartheta}_F(t)$ and $\bar{h}_F(\bar{\vartheta}_F)$, while the stars are the values recovered by a numerical simulation of the complete model with $a = 1$, $b = 1.4$, $Bo = 1000$, $\delta = 10^{-2}$, precursor film $h_{pr} = 0.02$ and $\vartheta_0 = 10^\circ$.

thickness:

$$\bar{\vartheta}_F = \vartheta_0 \left(\frac{2}{3} \left(\frac{1}{a^2} + \frac{1}{b^2} \right) t \right)^{1/4}, \quad \bar{h}_F = \left(\frac{\vartheta_0}{\bar{\vartheta}_F} \right)^2. \quad (5.12a,b)$$

The azimuth-averaged numerical solution of (5.11) and the analytical approximation (5.12a,b) are reported in figure 15, displaying a good agreement for low values of ϑ_0 and large values of a , while the results start to diverge for large ϑ_0 and small a .

Figure 16 shows the evolution of the front position and thickness with time, obtained from a numerical simulation of the complete model with $a = 1$, $b = 1.4$, $Bo = 1000$, $\delta = 10^{-2}$, precursor film $h_{pr} = 0.02$ and $\vartheta_0 = 10^\circ$. The values of front position and thickness are averaged and compared with the analytical prediction. The analytical and numerical simulation results show similar trends. However, at large times, the modulations of the front are very large and the front travels much faster along the shorter axis than along the longer one.

The spreading problem on an ellipsoid is characterized by a different front speed along the azimuthal direction, which leads to an accumulation of fluid and a faster spreading along the smaller axis. Peaks of large thickness form together with a modulation of the front, prior to any fingering instability. These modulations are similar to those observed in the previous section for the drainage solution. As already explained, larger velocities induce transport of fluid from regions of lower velocity to regions of larger velocity. As a result, fluid accumulates and forms the observed peaks of large thickness. These velocity differences lead to a progressively more pronounced bending of the front. Therefore, a fingering instability analysis necessarily needs to consider the non-uniform spreading of the fluid along the ellipsoid, which may lead to the preferential formation of fingers. While this analysis focused on the spreading in the absence of surface tension, further studies may involve the formation of fingers resulting from the driven contact-line instability.

In this section, we described the drainage and spreading solution for the coating on an ellipsoid. We obtained an analytical solution that compares well with the numerical one. We showed the potential of general coordinates and asymptotic expansions to obtain a two-dimensional analytical solution suitable for a physical interpretation of the drainage

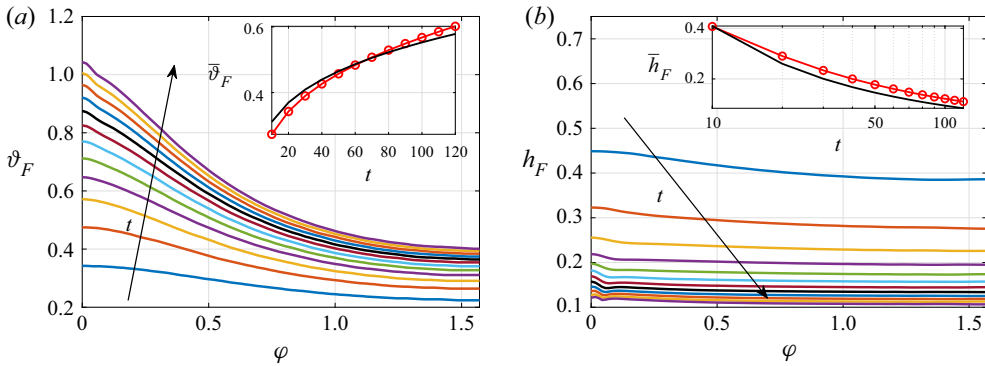


Figure 16. Maximum thickness (a) position and (b) value recovered from the numerical spreading simulation with $a = 1$, $b = 1.4$, $Bo = 1000$, $\delta = 10^{-2}$, precursor film $h_{pr} = 0.02$ and $\vartheta_0 = 10^\circ$. Different colours denote different times $10 \leq t \leq 120$, with step size $\Delta t = 10$. In the insets, we report a comparison between theoretical (black dashed line) and numerical (red dots) (a) average front position and (b) average front thickness.

and spreading process, in complement to the previous results for axisymmetric geometries. A large-time solution characterized by the separation of temporal and the two spatial dependencies was obtained. Modulations of the drainage solution and spreading front were explained in terms of the different slopes along the principal semiaxes, which induce an accumulation of fluid along the minor axis.

6. An experimental comparison

Our work focuses on developing analytical and numerical treatments of gravity-driven coatings on curved substrates. In this section, we compare our predictions with experiments. Rather than using Newtonian fluids, we use curable elastomers which drain until they solidify (Lee *et al.* 2016; Jones *et al.* 2021). As shown in Lee *et al.* (2016), this allows us to easily measure the final film thickness distribution by peeling off the solidified layer. Moreover, because of the large amount of fluid poured on the surface (20 g, leading to an initial thickness of ≈ 2 mm) and since the time required for the elastomer to solidify (~ 10 min) is much longer than the characteristic drainage time ($\tau \sim 10$ s), the solidified film thickness becomes insensitive to initial condition and does not depend on the pouring condition (see Lee *et al.* 2016). The experimental film thickness is compared with the late-time drainage solution, here modified to account for the change of viscosity of the elastomer melt over time (Lee *et al.* 2016; Jones *et al.* 2021). The experimental procedure is shown in figure 17 (and supplementary movie 1). We start by 3-D printing a mould with the desired geometry (Anycubic i3 Mega). The resulting surface is rough, with vertical steps of the order of the printer layer height: 0.1 mm (figure 17a). We smooth the surface by applying a first coating using a rapidly curing elastomer (Zhermack VPS-16, see Jones *et al.* (2021) for more details on the elastomer mixing procedure). This first layer is sufficiently thin compared with the substrate characteristic size ($\hat{h}/R \sim 10^{-3}$) so that we assume that the substrate curvature remains unchanged after coating. After solidification of the first layer (figure 17b), we proceed to the experiment and coat the sample with a second layer of elastomer (Zhermack VPS-32, figure 17c). After solidification of the second layer, thin strips of the solid shell (containing both layers) are cut, peeled from the substrate and imaged with a microscope (figure 17d). Dyes are mixed to both elastomers to enhance contrast, thereby allowing us to automatically extract the second layer thickness

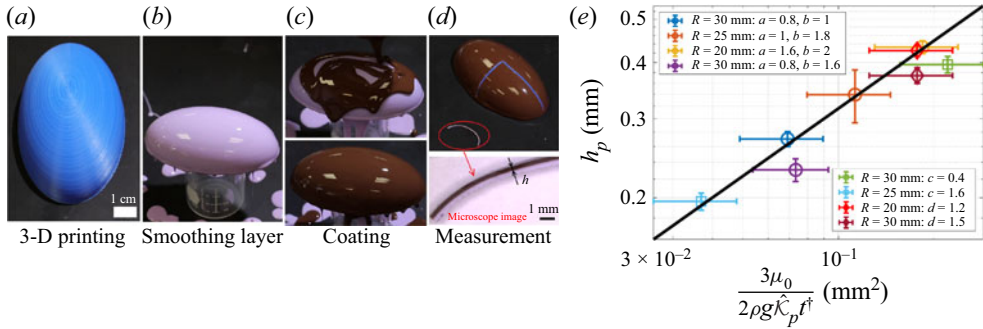


Figure 17. Different steps of the experimental procedure. (a) The 3-D printing of the moulds. (b) Smoothing of the mould via a first layer of polymer. (c) Coating and curing of the second layer. (d) Peeling of a thin stripe, whose thickness is measured through a microscope. The thickness of the second layer is compared with the analytical and numerical solutions. (e) Pole thickness, measurements for ellipsoids (circles), spheroids (squares) and tori (diamonds). The black line denotes the theoretical prediction.

as a function of the arclength $\hat{h}(\hat{s})$. The errors introduced through the cutting procedure and subsequent image analysis are smoothed by binning the thickness over 50 pixels in the horizontal direction. The standard deviation within each bin defines the experimental uncertainty. Finally, we map the dimensionless arclength s back to the zenith angle ϑ with the relation

$$s(\vartheta) = \int_0^\vartheta \sqrt{a^2 \sin^2(\vartheta') \cos^2 \varphi + b^2 \sin^2(\vartheta') \sin^2 \varphi + c^2 \cos^2 \vartheta'} \, d\vartheta'. \quad (6.1)$$

In all cases considered, the Bond number is in the range $177 < Bo = R^2/\ell_c^2 < 400$, where $\ell_c \approx 1.5 \text{ mm}$ is the capillary length of the polymer, while the final thickness is of order 10^{-1} mm , leading to $\delta \sim 10^{-2} - 10^{-3}$. These values of Bo and δ ensure the accuracy of the drainage solution everywhere except close to the edge of the mould where capillary effects play a central role by creating a rim or bead. We exclude from our results this rim, intrinsically induced by capillarity. Following the results of the asymptotic expansion for $\vartheta \ll 1$, the dimensional large-time thickness can be written as $\hat{h} = h_p f(\text{geometry})$, where f embeds the spatial distribution and depends only on the geometry, and h_p is the thickness at the pole which depends on the rheology of the polymer melt during the drainage. For a Newtonian fluid the pole thickness is given by (2.11), or in dimensional units $h_p = \sqrt{3\mu/2\rho g \hat{K}_p t}$ with \hat{K}_p the dimensional pole curvature. For a solidifying elastomer, we must account for the change of viscosity of the melt during curing $\mu(t)$ and the pole thickness is given by

$$h_p = \sqrt{\frac{3}{2\rho g \hat{K}_p \int_{\tau_w}^\infty \frac{1}{\mu(t)} dt}}, \quad (6.2)$$

where τ_w is the time after mixing at which we start the drainage, $\tau_w \approx 6 \text{ min}$ in our experiments. The rheology of VPS-32 is reported in Lee *et al.* (2016)

$$\mu(t) = \begin{cases} \mu_0 \exp(\beta t), & \text{if } t \leq \tau_c, \\ \mu_1 t^\alpha, & \text{if } t > \tau_c, \end{cases} \quad (6.3)$$

Polymer	μ_0 (Pa s)	α	β ($\times 10^{-3}$)	τ_c (s)
VPS-32	7.1 ± 0.2	5.3 ± 0.7	2.06 ± 0.09	574 ± 11

Table 1. Properties of VPS-32, extracted from Lee *et al.* (2016).

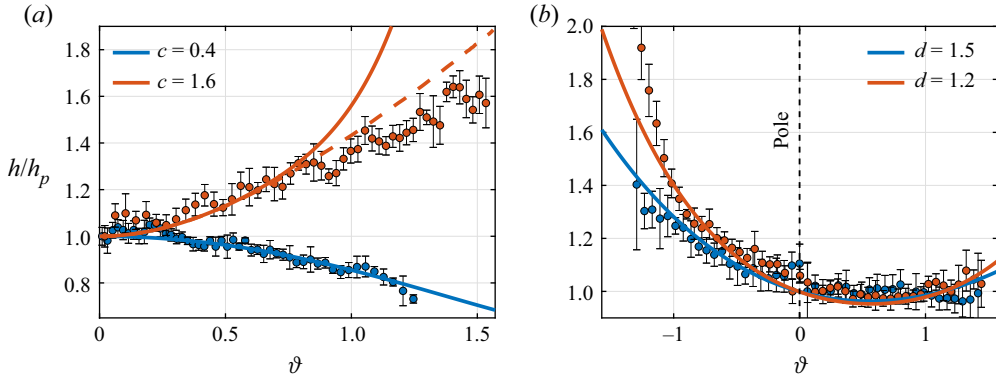


Figure 18. Comparison between experimental measurements of h/h_p (coloured dots) and the theoretical prediction from (a) § 3.1 for two spheroids with $c = 0.4$ and $R = 30$ mm, $c = 1.6$ and $R = 20$ mm, and (b) § 4 for two tori with $R = 30$ mm, and $d = 1.2, 1.5$. The coloured solid thick lines denote the analytical solutions, and the dashed ones the numerical solutions.

with $\mu_1 = \mu_0 \exp(\beta\tau_c)\tau_c^{-\alpha}$. Upon integration, the pole thickness reads $h_p = \sqrt{3\mu_0/(2\rho g \widehat{\mathcal{K}}_p t^\dagger)}$, where $t^\dagger = \{(e^{-\beta\tau_w} - e^{-\beta\tau_c})/\beta\} + \{\tau_c e^{-\beta\tau_c}/(\alpha - 1)\}$. The values of the parameters, together with the uncertainties, are reported in table 1. In figure 17(e), the theoretical prediction is compared with the experimental measurements for different substrates, showing an overall good agreement, valid for all substrates as highlighted in § 2.3.

In the following, we rescale the measured thickness with the pole thickness so as to compare the spatial distributions, independently of the fluid rheology, i.e. $\hat{h}/h_p = f(\text{geometry})$. Figure 18 shows experimental measurements (dots) for two spheroids (a) and two tori (b) compared with the numerical (dashed line) and analytical (solid line) solutions at order $O(\vartheta^6)$ for the spheroids, and $O(\vartheta^4)$ for the tori. In all cases, the trend of analytical, numerical and experimental results are similar. For the spheroids, the thickness decreases when moving from the apex to the equator for $c = 0.4$. Instead, for $c = 1.6$ the thickness is found to increase. For the latter case, a favourable agreement for large ϑ is obtained with the numerical solution (dashed line), in agreement with previous discussions. Similar favourable agreements are obtained for tori. In particular, the analytical solution captures the increase in thicknesses observed for $\vartheta < 0$, i.e. in the inner part of the torus. In figure 19, we show experimental measurements (dots) for the thickness along the long ($\varphi = \pi/2$) and short ($\varphi = 0$) axes of ellipsoids with various aspect ratios and compare them with the numerical (dashed lines) and analytical (solid lines) solutions. We recover the three thickness distributions predicted, i.e. (a) thickness increasing both on the short and long axes for $a, b \gtrsim 1.35$, (b,c) thickness increasing along the short axis and decreasing on the long axis for $a \gtrsim 1.35 \gtrsim b$, (d) thickness decreasing along

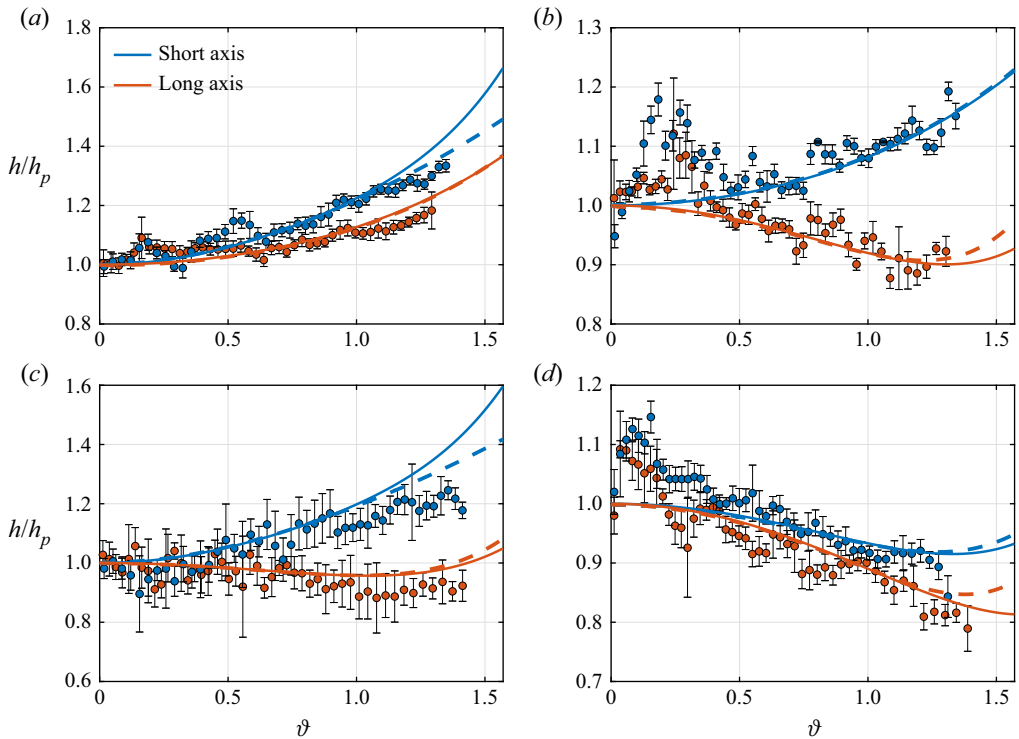


Figure 19. Comparison between analytical (solid lines), numerical (dashed lines) solutions and experimental measurements, in analogy with figure 19, for ellipsoids with (a) $a = 0.8$, $b = 1$ and $R = 30$ mm, (b) $a = 1$, $b = 1.8$ and $R = 25$ mm, (c) $a = 0.8$, $b = 1.6$ and $R = 30$ mm, (d) $a = 1.6$, $b = 2$ and $R = 20$ mm.

both axes $a, b \gtrsim 1.35$. In all cases, the experimental measurements show the same trends as the numerical solutions and highlight the different thickness distributions previously described. However, some local discrepancies can be noticed. With reference to figure 18, the thickness predicted from the nonlinear simulations for case $c = 1.6$ of panel (a) is larger than the measured one, in the vicinity of the equator, while in case $d = 1.2$ of figure 18(b) the measured thickness is larger than the predicted one. These discrepancies may be induced by the previously described edge effect that creates a rim or bead, where capillarity and hydrostatic effects dominate. Cases (b) and (d) of figure 19 instead show a peak in the thickness for small ϑ , with experimental values larger than the ones predicted by the theoretical and numerical results. These thickness variations are likely due to defects in the cutting process (shown in supplementary movie 1), or to the target shape not being exactly attained, even after the first coating employed to smoothen the stepped surface in the vicinity of the pole, where the substrate inclination is small.

7. Conclusion

This work studied the coating problem on a generic substrate with a focus on three-dimensional drainage and spreading. We analysed different substrate geometries and derived analytical solutions for the drainage and spreading of an initial volume of fluid, under the assumption of very large Bond number and very thin film compared with the substrate characteristic length. We derived a general solution for the thickness evolution on a local maximum of the substrate. The thickness was found to be inversely proportional to

the square root of the mean curvature at the pole, i.e. $h = \sqrt{3/(2\mathcal{K}_p t)}$. The latter represents how the components of the gravitational field, tangential to the substrate, vary across the surface in the vicinity of the pole. Therefore, a larger drainage and a faster decrease of the thickness are obtained with increasing mean curvature. We then investigated the role of the substrate geometry in modifying the thickness distribution away from the local maximum. We considered as a test case the coating on a spheroid of dimensionless height c , whose solution was derived through an asymptotic expansion in the vicinity of the pole. For $c < c^*$, the thickness decreases as we move away from the pole while it increases for $c > c^*$. These thickness variations result from a competition between the slope and curvature which balance each other for $c = c^* = \sqrt{2/3}$. In particular, the fluid tends to accumulate in regions of lower curvature while a slope increase induces film thickening. The drainage solution was then employed to study the spreading of an initial volume of fluid contained in a region close to the pole. The spreading velocity was found to increase with the spheroid height. We related this behaviour to the increase of the drainage gravity component with c in the vicinity of the pole. We then studied the coating of a substrate in which the symmetry of the spreading is broken, i.e. the torus. The coating solution presented much larger values of the thickness on the inner part than on the outer part. The inner part presents a decreasing mean curvature, thus leading to larger values of the thickness than those observed on the outer part, where the mean curvature slightly increases since gravity is symmetric. The spreading of an initial volume of fluid occurred much faster on the inner region than on the outer region since the area to be invaded is smaller on the inner region, giving rise to two different spreading fronts. We concluded the analysis by applying the method to the three-dimensional spreading problem on a non-axisymmetric ellipsoidal substrate, i.e. with three different axes. We first derived a large-time analytical drainage solution which agrees well with the numerical simulations. Depending on the ellipsoid geometry, the thickness can increase or decrease away from the pole, with a behaviour similar to the spheroid one along the principal axes. The solution was characterized by π -periodic modulations along the azimuthal direction, related to the different drainage along the two principal axes of the ellipsoid, which tend to move fluid from the major axis to the minor one. These modulations reflect in a spreading which does not occur uniformly along the azimuthal direction, but shows an accumulation of fluid and a faster spreading along the shorter axis. These modulations in the front position occur prior to any fingering instability. We obtained a scaling for the average front which fairly agrees with numerical results. We finally compared the spreading results with experimental measurements and found a good agreement in terms of spatial distributions.

The scope of the present work is to give a coherent and formal framework for the study of the drainage and coating on generic substrates based on the generalization and targeted application of previous analytical developments. These analyses show a crucial effect of the substrate curvature in defining the leading-order thickness distribution and the spreading front of a gravity-driven coating. The natural extension of this work is the focus on the destabilization of these spreading fronts. While previous works focused on the fingering instability of two-dimensional fronts (Troian *et al.* 1989a; Bertozzi & Brenner 1997; Balestra *et al.* 2019), similar studies in which the primary front can bend and evolve together with fingering instabilities still need to be pursued. These analyses are not necessarily constrained by the considered configuration, but can be also extended to converging flows and more complex substrates. Besides, the performed analyses are valid in the absence of capillary and hydrostatic pressure effects. This assumption is respected when the film is very thin and the substrate does not present regions with infinite or zero curvature. If one of these hypotheses is violated, then other effects may play a crucial role.

Hydrostatic pressure gradients become non-negligible if the film becomes thicker or the substrate presents flat regions, e.g. a saddle point. Following the work of Lister (1992) for a flat substrate, the role of hydrostatic pressure gradients in these situations still needs to be investigated. These findings may find several applications both in environmental studies and thin film technologies. The interweaving between differential geometry and asymptotic theory showed great potential in the evaluation of analytical and numerical solutions for the coating on complex geometries, which may find further developments not only in the study of contact-line instabilities, but in several coating flow phenomena such as Marangoni, inertia-driven and Rayleigh–Taylor instabilities.

Supplementary material and movie. Supplementary material and movie are available at <https://doi.org/10.1017/jfm.2022.758>.

Acknowledgements. P.G.L. is grateful to A. Bongarzone for the precious suggestions regarding the ellipsoid analytical solution. P.G.L. also acknowledges S. Djambov for the fruitful discussions on the geometrical interpretation of the results.

Funding. This work was supported by the Swiss National Science Foundation (grant no. 200021_178971 to P.G.L.).

Declaration of interests. The authors report no conflict of interest.

Author ORCIDs.

- ✉ Pier Giuseppe Ledda <https://orcid.org/0000-0003-4435-8613>;
- ✉ M. Pezzulla <https://orcid.org/0000-0002-3165-8011>;
- ✉ E. Jambon-Puillet <https://orcid.org/0000-0003-2453-0578>;
- ✉ P.-T. Brun <https://orcid.org/0000-0002-4175-0604>;
- ✉ F. Gallaire <https://orcid.org/0000-0002-3029-1457>.

Appendix A. Spheroid: higher-order drainage problems

In this section, the higher-order drainage problems are described. We report only the ODE to be solved since their expressions are cumbersome. The ODE at $O(\vartheta^4)$ reads

$$\left. \begin{aligned} H_0^2 \left(\left(\frac{11c}{3} - 5c^3 \right) H_2 + 6cH_4 \right) + \frac{1}{36}c(48c^4 - 66c^2 + 19)H_0^3 + 6cH_0H_2^2 + H_4' &= 0, \\ H_4(0) &= 0. \end{aligned} \right\} \quad (A1a,b)$$

At $O(\vartheta^6)$, the problem reads

$$\begin{aligned} & -\frac{1}{3}cH_0H_2((21c^2 - 16)H_2 - 48H_4) \\ & + H_0^2 \left(-7c^3H_4 + \left(6c^5 - \frac{17c^3}{2} + \frac{13c}{5} \right) H_2 + \frac{16}{3}cH_4 + 8cH_6 \right) \end{aligned} \quad (A2)$$

$$+ \left(-\frac{5c^7}{3} + \frac{31c^5}{9} - \frac{257c^3}{120} + \frac{49c}{135} \right) H_0^3 + \frac{8}{3}cH_2^3 + H_6' = 0, \quad H_6(0) = 0. \quad (A3a,b)$$

Appendix B. Torus: drainage solution

Also in this section, we report only the problems when their relative solution is cumbersome. The problems for increasing orders read

$$H_0'(t) = -\frac{1}{3}H_0(t)^3, \quad H_0(0) = 1 \rightarrow H_0(t) = \frac{1}{\sqrt{\frac{2t}{3} + 1}}, \quad (B1a,b)$$

$$\left. \begin{aligned} H_1'(t) &= -\left(\frac{H_0(t)^3}{3d} + 2H_0(t)^2H_1(t)\right), \quad H_1(0) = 0, \\ \rightarrow H_1(t) &= \frac{-8\sqrt{3}t^3 - 36\sqrt{3}t^2 - 54\sqrt{3}t + 27\sqrt{2t+3} - 27\sqrt{3}}{5d(2t+3)^{7/2}}, \end{aligned} \right\} (B2)$$

$$\left. \begin{aligned} H_2'(t) &= -\left(-\frac{(d^2+2)H_0(t)^3}{6d^2} + \frac{H_0(t)^2(3dH_2(t) + H_1(t))}{d} + 3H_0(t)H_1(t)^2\right), \\ H_2(0) &= 0, \\ \rightarrow H_2(t) &= \frac{1}{50d^2(2t+3)^{11/2}} \left\{ 4\sqrt{3}(25d^2+62)t^5 + 30\sqrt{3}(25d^2+62)t^4 \right. \\ &\quad + 90\sqrt{3}(25d^2+62)t^3 + 27t^2(125\sqrt{3}d^2 + 8\sqrt{2t+3} + 310\sqrt{3}) \\ &\quad \left. + 81t(25\sqrt{3}d^2 + 8(\sqrt{2t+3} + 5\sqrt{3})) - 486(\sqrt{3} - \sqrt{2t+3}) \right\}, \end{aligned} \right\} (B3)$$

$$\left. \begin{aligned} 72d^3H_0(t)H_1H_2 - 6d^3H_0(t)^2H_1 + 36d^3H_0(t)^2H_3(t) + 12d^3H_1^3 + 9d^3H_3'(t) + 9d^2 \\ H_0(t)H_1^2 + 9d^2H_0(t)^2H_2 - 2d^2H_0(t)^3 - 9dH_0(t)^2H_1 + 3H_0(t)^3 = 0, \quad H_3(0) = 0, \end{aligned} \right\} (B4)$$

$$\begin{aligned} &720d^4H_0(t)H_1(t)H_3(t) - 60d^4H_0(t)H_1(t)^2 + 360d^4H_0(t)H_2(t)^2 - 60d^4H_0(t)^2H_2(t) \\ &+ 360d^4H_0(t)^2H_4(t) + d^4H_0(t)^3 + 360d^4H_1(t)^2H_2(t) + 72d^4H_4'(t) \\ &+ 144d^3H_0(t)H_1(t)H_2(t) - 48d^3H_0(t)^2H_1(t) + 72d^3H_0(t)^2H_3(t) + 24d^3H_1(t)^3 \\ &- 72d^2H_0(t)H_1(t)^2 - 72d^2H_0(t)^2H_2(t) + 20d^2H_0(t)^3 + 72dH_0(t)^2H_1(t) \\ &- 24H_0(t)^3 = 0, \quad H_4(0) = 0. \end{aligned} \quad (B5)$$

Appendix C. Ellipsoid: higher-order drainage solutions

The PDE for $H_4(\varphi, t)$ reads

$$\begin{aligned} &\frac{7 \cos(2\varphi)H_0^3}{36a^2} + \frac{\cos(2\varphi)H_0^3}{2a^6} + \frac{\cos(2\varphi)H_0^3}{6a^4b^2} + \frac{13 \cos(2\varphi)H_0^3}{18b^4} + \frac{\cos(4\varphi)H_0^3}{8a^6} + \frac{\cos(4\varphi)H_0^3}{6a^2b^2} \\ &+ \frac{\cos(4\varphi)H_0^3}{8b^6} + \frac{19H_0^3}{72a^2} - \frac{\cos(4\varphi)H_0^3}{12a^4} - \frac{13 \cos(2\varphi)H_0^3}{18a^4} - \frac{23H_0^3}{36a^4} + \frac{3H_0^3}{8a^6} - \frac{7 \cos(2\varphi)H_0^3}{36b^2} \\ &+ \frac{19H_0^3}{72b^2} - \frac{5H_0^3}{9a^2b^2} - \frac{\cos(4\varphi)H_0^3}{8a^4b^2} + \frac{7H_0^3}{24a^4b^2} - \frac{\cos(4\varphi)H_0^3}{12b^4} - \frac{23H_0^3}{36b^4} - \frac{\cos(2\varphi)H_0^3}{6a^2b^4} \end{aligned}$$

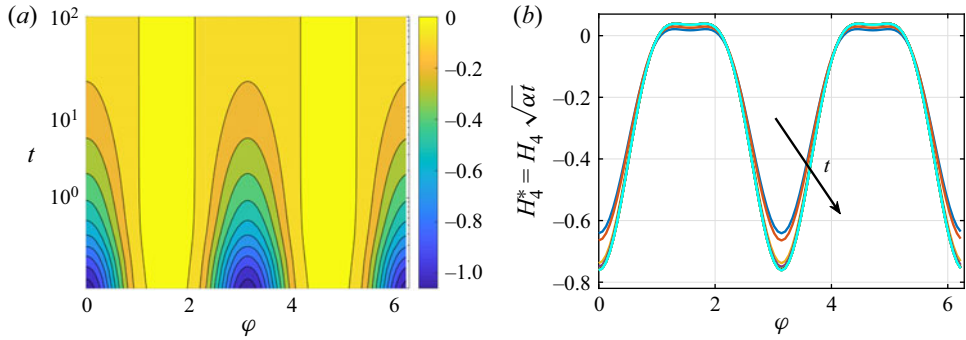


Figure 20. Drainage on an ellipsoid with $a = 0.5$ and $b = 1.5$. (a) Spatio-temporal evolution of H_4 : iso-contours of H_2 in the (φ, t) plane. (b) Second-order correction $H_4^* = H_4/H_0 \approx H_4\sqrt{\alpha t}$ as a function of φ at different times: $t = 0.4$ (blue), $t = 1$ (orange), $t = 5$ (yellow), $t = 10$ (purple), $t = 20$ (green), $t = 30$ (cyan), $t = 40$ (maroon), $t = 50$ (black), $t = 60$ (red), $t = 70$ (light green), $t = 80$ (dark blue), $t = 90$ (light yellow), $t = 100$ (light cyan).

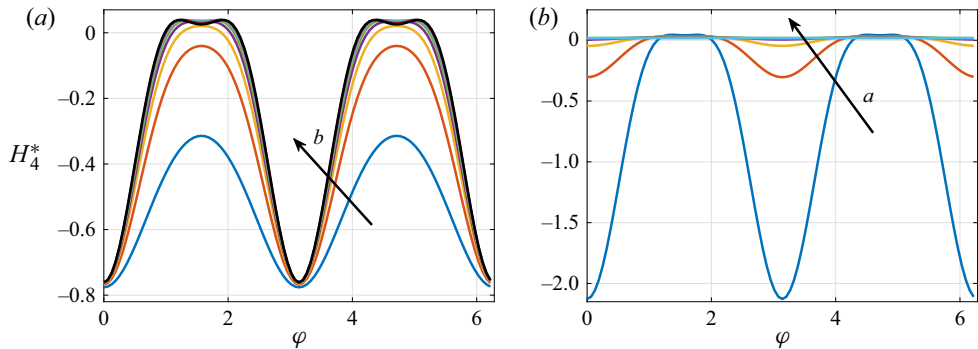


Figure 21. (a) Fourth-order correction $H_4^* = H_4/H_0 \approx H_4\sqrt{\alpha t}$ as a function of φ at $t = 100$, for $a = 0.5$ and increasing b : $b = 0.6$ (blue), $b = 0.8$ (orange), $b = 1$ (yellow), $b = 1.2$ (purple), $b = 1.4$ (green), $b = 1.6$ (cyan), $b = 1.8$ (maroon), $b = 2$ (black). (b) Second-order correction H_4^* as a function of φ at $t = 100$, for $b = 1.5$ and increasing a : $a = 0.4$ (blue), $a = 0.6$ (orange), $a = 0.8$ (yellow), $a = 1$ (purple), $a = 1.2$ (green), $a = 1.4$ (cyan).

$$\begin{aligned}
 & -\frac{\cos(4\varphi)H_0^3}{8a^2b^4} + \frac{7H_0^3}{24a^2b^4} - \frac{\cos(2\varphi)H_0^3}{2b^6} + \frac{3H_0^3}{8b^6} + \frac{4\cos(2\varphi)H_2H_0^2}{3a^2} + \frac{2\cos(2\varphi)H_2H_0^2}{b^4} \\
 & + \frac{\cos(4\varphi)H_2H_0^2}{2a^2b^2} + \frac{11H_2H_0^2}{6a^2} + \frac{11H_2H_0^2}{6b^2} + \frac{2\cos(2\varphi)H_4H_0^2}{a^2} + \frac{3H_4H_0^2}{a^2} + \frac{3H_4H_0^2}{b^2} \\
 & + \frac{\cos(2\varphi)\sin(2\varphi)\frac{\partial H_2}{\partial\varphi}H_0^2}{4a^4} + \frac{\cos(2\varphi)\sin(2\varphi)\frac{\partial H_2}{\partial\varphi}H_0^2}{4b^4} + \frac{\sin(2\varphi)\frac{\partial H_2}{\partial\varphi}H_0^2}{4a^4} \\
 & + \frac{\sin(2\varphi)\frac{\partial H_2}{\partial\varphi}H_0^2}{4b^2} + \frac{\sin(2\varphi)\frac{\partial H_4}{\partial\varphi}H_0^2}{2b^2} - \frac{\sin(2\varphi)\frac{\partial H_4}{\partial\varphi}H_0^2}{2a^2} - \frac{\sin(2\varphi)\frac{\partial H_2}{\partial\varphi}H_0^2}{4a^2} \\
 & - \frac{2\cos(2\varphi)H_2H_0^2}{a^4} - \frac{\cos(4\varphi)H_2H_0^2}{4a^4} - \frac{7H_2H_0^2}{4a^4} - \frac{2\cos(2\varphi)H_4H_0^2}{b^2} - \frac{4\cos(2\varphi)H_2H_0^2}{3b^2}
 \end{aligned}$$

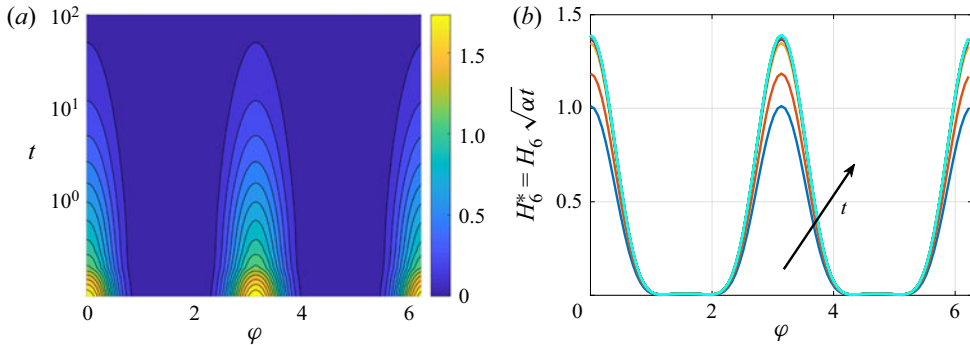


Figure 22. Drainage on an ellipsoid with $a = 0.5$ and $b = 1.5$. (a) Spatio-temporal evolution of H_6 : iso-contours of H_6 in the (φ, t) plane. (b) Second-order correction $H_6^* = H_6/H_0 \approx H_6\sqrt{\alpha t}$ as a function of φ at different times: $t = 0.4$ (blue), $t = 1$ (orange), $t = 5$ (yellow), $t = 10$ (purple), $t = 20$ (green), $t = 30$ (cyan), $t = 40$ (maroon), $t = 50$ (black), $t = 60$ (red), $t = 70$ (light green), $t = 80$ (dark blue), $t = 90$ (light yellow), $t = 100$ (light cyan).

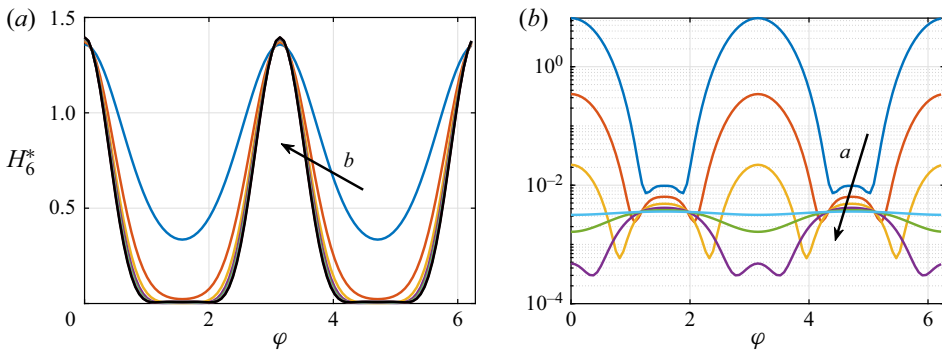


Figure 23. (a) Sixth-order correction $H_6^* = H_6/H_0 \approx H_6\sqrt{\alpha t}$ as a function of φ at $t = 100$, for $a = 0.5$ and increasing b : $b = 0.6$ (blue), $b = 0.8$ (orange), $b = 1$ (yellow), $b = 1.2$ (purple), $b = 1.4$ (green), $b = 1.6$ (cyan), $b = 1.8$ (maroon), $b = 2$ (black). (b) Second-order correction H_6^* as a function of φ at $t = 100$, for $b = 1.5$ and increasing a : $a = 0.4$ (blue), $a = 0.6$ (orange), $a = 0.8$ (yellow), $a = 1$ (purple), $a = 1.2$ (green), $a = 1.4$ (cyan).

$$\begin{aligned}
 & -\frac{3H_2H_0^2}{2a^2b^2} - \frac{\cos(2\varphi)\sin(2\varphi)\frac{\partial H_2}{\partial\varphi}H_0^2}{2a^2b^2} - \frac{\cos(4\varphi)H_2H_0^2}{4b^4} - \frac{7H_2H_0^2}{4b^4} - \frac{\sin(2\varphi)\frac{\partial H_2}{\partial\varphi}H_0^2}{4b^4} \\
 & + \frac{2\cos(2\varphi)H_2^2H_0}{a^2} + \frac{3H_2^2H_0}{a^2} + \frac{3H_2^2H_0}{b^2} + \frac{H_2\sin(2\varphi)\frac{\partial H_2}{\partial\varphi}H_0}{b^2} - \frac{H_2\sin(2\varphi)\frac{\partial H_2}{\partial\varphi}H_0}{a^2} \\
 & - \frac{2\cos(2\varphi)H_2^2H_0}{b^2} + \frac{\partial H_4}{\partial t} = 0, \tag{C1}
 \end{aligned}$$

whose numerical solution is reported in figures 20 and 21. Figure 20(b) shows that the values of the rescaled fourth-order solution $H_4^* = H_4\sqrt{\alpha t}$ collapse to the same curve as time increases, thus suggesting that also in this case a large-time separation of variables is possible.

Because of its size, we do not write the PDE for H_6 here; however, the solutions are shown in figures 22 and 23. In analogy with the solutions at order $O(\vartheta^2)$ and $O(\vartheta^4)$,

the behaviour of the large-time solution suggests that a solution $H_n^*(\varphi) = H_n(\varphi, t)/H_0(t)$ satisfies the problem.

REFERENCES

- ACHESON, D.J. 1990 *Elementary Fluid Dynamics*. Oxford University Press.
- ANCEY, C. 2007 Plasticity and geophysical flows: a review. *J. Non-Newtonian Fluid Mech.* **142** (1–3), 4–35.
- BALESTRA, G., BADAOU, M., DUCIMETIÈRE, Y.-M. & GALLAIRE, F. 2019 Fingering instability on curved substrates: optimal initial film and substrate perturbations. *J. Fluid Mech.* **868**, 726–761.
- BALESTRA, G., KOFMAN, N., BRUN, P.-T., SCHEID, B. & GALLAIRE, F. 2018a Three-dimensional Rayleigh–Taylor instability under a unidirectional curved substrate. *J. Fluid Mech.* **837**, 19–47.
- BALESTRA, G., NGUYEN, D.M.-P. & GALLAIRE, F. 2018b Rayleigh–Taylor instability under a spherical substrate. *Phys. Rev. Fluids* **3** (8), 084005.
- BALMFORTH, N.J., BURBIDGE, A.S., CRASTER, R.V., SALZIG, J. & SHEN, A. 2000 Visco-plastic models of isothermal lava domes. *J. Fluid Mech.* **403**, 37–65.
- BALMFORTH, N.J., CRASTER, R.V., RUST, A.C. & SASSI, R. 2006 Viscoplastic flow over an inclined surface. *J. Non-Newtonian Fluid Mech.* **139** (1–2), 103–127.
- BALMFORTH, N.J., CRASTER, R.V. & SASSI, R. 2002 Shallow viscoplastic flow on an inclined plane. *J. Fluid Mech.* **470**, 1–29.
- BALMFORTH, N.J. & KERSWELL, R.R. 2005 Granular collapse in two dimensions. *J. Fluid Mech.* **538**, 399–428.
- BERTAGNI, M.B. & CAMPOREALE, C. 2021 The hydrodynamic genesis of linear karren patterns. *J. Fluid Mech.* **913**, A34.
- BERTAGNI, M.B. & CAMPOREALE, C. 2017 Nonlinear and subharmonic stability analysis in film-driven morphological patterns. *Phys. Rev. E* **96** (5), 053115.
- BERTOZZI, A.L. & BRENNER, M.P. 1997 Linear stability and transient growth in driven contact lines. *Phys. Fluids* **9** (3), 530–539.
- CAMPOREALE, C. 2015 Hydrodynamically locked morphogenesis in karst and ice flutings. *J. Fluid Mech.* **778**, 89–119.
- CAMPOREALE, C. & RIDOLFI, L. 2012 Hydrodynamic-driven stability analysis of morphological patterns on stalactites and implications for cave paleoflow reconstructions. *Phys. Rev. Lett.* **108** (23), 238501.
- CHANDRASEKHAR, S. 2013 *Hydrodynamic and Hydromagnetic Stability*. Courier Corporation.
- COUDER, Y., FORT, E., GAUTIER, C.-H. & BOUDAUD, A. 2005 From bouncing to floating: noncoalescence of drops on a fluid bath. *Phys. Rev. Lett.* **94**, 177801.
- CRASTER, R.V. & MATAR, O.K. 2009 Dynamics and stability of thin liquid films. *Rev. Mod. Phys.* **81** (3), 1131.
- DESERNO, M. 2004 Notes on differential geometry. Available at: https://www.cmu.edu/biolphys/deserno/pdf/diff_geom.pdf.
- DIDDEN, N. & MAXWORTHY, T. 1982 The viscous spreading of plane and axisymmetric gravity currents. *J. Fluid Mech.* **121**, 27–42.
- DURUK, S., BOUJO, E. & SELLIER, M. 2021 Thin liquid film dynamics on a spinning spheroid. *Fluids* **6** (9), 318.
- FERMIGIER, M., LIMAT, L., WESFREID, J.E., BOUDINET, P. & QUILLIET, C. 1992 Two-dimensional patterns in Rayleigh–Taylor instability of a thin layer. *J. Fluid Mech.* **236**, 349–383.
- GRATTON, J. & MINOTTI, F. 1990 Self-similar viscous gravity currents: phase-plane formalism. *J. Fluid Mech.* **210**, 155–182.
- HOSOI, A.E. & BUSH, J.W.M. 2001 Evaporative instabilities in climbing films. *J. Fluid Mech.* **442**, 217.
- HOULT, D.P. 1972 Oil spreading on the sea. *Annu. Rev. Fluid Mech.* **4** (1), 341–368.
- HOWELL, P.D. 2003 Surface-tension-driven flow on a moving curved surface. *J. Engng Maths* **45** (3), 283–308.
- HUPPERT, H.E. 1982a Flow and instability of a viscous current down a slope. *Nature* **300** (5891), 427–429.
- HUPPERT, H.E. 1982b The propagation of two-dimensional and axisymmetric viscous gravity currents over a rigid horizontal surface. *J. Fluid Mech.* **121**, 43–58.
- HUPPERT, H.E. 1986 The intrusion of fluid mechanics into geology. *J. Fluid Mech.* **173**, 557–594.
- HUPPERT, H.E. 2006 Gravity currents: a personal perspective. *J. Fluid Mech.* **554**, 299–322.
- HUPPERT, H.E. & SIMPSON, J.E. 1980 The slumping of gravity currents. *J. Fluid Mech.* **99** (4), 785–799.
- IRGENS, F. 2019 *Tensor Analysis*. Springer.
- JAMBON-PUILLET, E., LEDDA, P.G., GALLAIRE, F. & BRUN, P.-T. 2021 Drops on the underside of a slightly inclined wet substrate move too fast to grow. *Phys. Rev. Lett.* **127**, 044503.

- JEFFREYS, H. 1930 The draining of a vertical plate. *Math. Proc. Camb. Phil. Soc.* **26** (2), 204–205.
- JONES, T.J., JAMBON-PUILLET, E., MARTHELOT, J. & BRUN, P.-T. 2021 Bubble casting soft robotics. *Nature* **599** (7884), 229–233.
- KAPITZA, P.L. 1948 Wave flow of thin layers of viscous liquid. *Zh. Eksp. Teor. Fiz.* **18**, 3–28.
- KAPITZA, P.L. & KAPITZA, S.P. 1965 Wave flow of thin layers of a viscous fluid: experimental study of undulatory flow conditions. In *Collected Papers of PL Kapitza* (ed. D. Ter Haar), vol. 2. Pergamon.
- KEULEGAN, G.H. 1957 An experimental study of the motion of saline water from locks into fresh water channels. *Nat. Bur. Stand. Rept. Tech. Rep.* 5168.
- KONDIC, L. 2003 Instabilities in gravity driven flow of thin fluid films. *SIAM Rev.* **45** (1), 95–115.
- KONDIC, L. & DIEZ, J. 2002 Flow of thin films on patterned surfaces: controlling the instability. *Phys. Rev. E* **65**, 045301.
- LANDAU, L.D. & LEVICH, B. 1942 Dragging of a liquid by a moving plate. *Acta Physicochim. USSR* **17**, 141–153.
- LEDDA, P.G., BALESTRA, G., LERISSON, G., SCHEID, B., WYART, M. & GALLAIRE, F. 2021 Hydrodynamic-driven morphogenesis of karst draperies: spatio-temporal analysis of the two-dimensional impulse response. *J. Fluid Mech.* **910**, A53.
- LEDDA, P.G. & GALLAIRE, F. 2021 Secondary instability in thin film flows under an inclined plane: growth of lenses on spatially developing rivulets. *Proc. R. Soc. Lond. A* **477** (2251), 20210291.
- LEDDA, P.G., LERISSON, G., BALESTRA, G. & GALLAIRE, F. 2020 Instability of a thin viscous film flowing under an inclined substrate: the emergence and stability of rivulets. *J. Fluid Mech.* **904**, A23.
- LEE, A., BRUN, P.-T., MARTHELOT, J., BALESTRA, G., GALLAIRE, F. & REIS, P.M. 2016 Fabrication of slender elastic shells by the coating of curved surfaces. *Nat. Commun.* **7** (1), 11155.
- LERISSON, G., LEDDA, P.G., BALESTRA, G. & GALLAIRE, F. 2019 Dripping down the rivulet. *Phys. Rev. Fluids* **4**, 100504.
- LERISSON, G., LEDDA, P.G., BALESTRA, G. & GALLAIRE, F. 2020 Instability of a thin viscous film flowing under an inclined substrate: steady patterns. *J. Fluid Mech.* **898**, A6.
- LIN, T.-S., DIJKSMAN, J.A. & KONDIC, L. 2021 Thin liquid films in a funnel. *J. Fluid Mech.* **924**, A26.
- LISTER, J.R. 1992 Viscous flows down an inclined plane from point and line sources. *J. Fluid Mech.* **242**, 631–653.
- MAYO, L.C., MCCUE, S.W., MORONEY, T.J., FORSTER, W.A., KEMPTHORNE, D.M., BELWARD, J.A. & TURNER, I.W. 2015 Simulating droplet motion on virtual leaf surfaces. *R. Soc. Open. Sci.* **2** (5), 140528.
- MEAKIN, P. & JAMTVEIT, B. 2010 Geological pattern formation by growth and dissolution in aqueous systems. *Proc. R. Soc. Lond. A* **466** (2115), 659–694.
- ORON, A. 2000 Nonlinear dynamics of three-dimensional long-wave Marangoni instability in thin liquid films. *Phys. Fluids* **12** (7), 1633–1645.
- ORON, A., DAVIS, S.H. & BANKOFF, S.G. 1997 Long-scale evolution of thin liquid films. *Rev. Mod. Phys.* **69** (3), 931.
- QIN, J., XIA, Y.-T. & GAO, P. 2021 Axisymmetric evolution of gravity-driven thin films on a small sphere. *J. Fluid Mech.* **907**, A4.
- RAYLEIGH, 1882 Investigation of the character of the equilibrium of an incompressible heavy fluid of variable density. *Proc. Lond. Math. Soc.* **s1-14** (1), 170–177.
- ROBERTS, A.J. & LI, Z. 2006 An accurate and comprehensive model of thin fluid flows with inertia on curved substrates. *J. Fluid Mech.* **553**, 33–73.
- ROY, R.V., ROBERTS, A.J. & SIMPSON, M.E. 2002 A lubrication model of coating flows over a curved substrate in space. *J. Fluid Mech.* **454**, 235–261.
- SCHEID, B. 2013 *Rivulet Structures in Falling Liquid Films*, pp. 435–441. Springer.
- SCHWARTZ, L.W. & ROY, R.V. 2004 Theoretical and numerical results for spin coating of viscous liquids. *Phys. Fluids* **16** (3), 569–584.
- SCRIVEN, L.E. 1988 Physics and applications of dip coating and spin coating. *MRS Online Proc. Library (OPL)* **121**, 717–729.
- SHORT, M.B., BAYGENTS, J.C., BECK, J.W., STONE, D.A., TOOMEY III, R.S. & GOLDSTEIN, R.E. 2005 Stalactite growth as a free-boundary problem: a geometric law and its platonic ideal. *Phys. Rev. Lett.* **94** (1), 018501.
- SIMPSON, J.E. 1982 Gravity currents in the laboratory, atmosphere, and ocean. *Annu. Rev. Fluid Mech.* **14** (1), 213–234.
- SMITH, S.H. 1969 On initial value problems for the flow in a thin sheet of viscous liquid. *Z. Angew. Math. Phys.* **20** (4), 556–560.
- TAKAGI, D. & HUPPERT, H.E. 2010 Flow and instability of thin films on a cylinder and sphere. *J. Fluid Mech.* **647**, 221–238.

- TAYLOR, G.I. 1950 The instability of liquid surfaces when accelerated in a direction perpendicular to their planes. I. *Proc. R. Soc. Lond. A* **201** (1065), 192–196.
- THIFFEAULT, J.-L. & KAMHAWI, K. 2006 Transport in thin gravity-driven flow over a curved substrate. [arXiv:nlin/0607075](https://arxiv.org/abs/nlin/0607075).
- TROIAN, S.M., HERBOLZHEIMER, E., SAFRAN, S.A. & JOANNY, J.F. 1989*a* Fingering instabilities of driven spreading films. *Europhys. Lett.* **10** (1), 25.
- TROIAN, S.M., WU, X.L. & SAFRAN, S.A. 1989*b* Fingering instability in thin wetting films. *Phys. Rev. Lett.* **62** (13), 1496.
- WEINSTEIN, S.J. & RUSCHAK, K.J. 2004 Coating flows. *Annu. Rev. Fluid Mech.* **36**, 29–53.
- WRAY, A.W., PAPAGEORGIOU, D.T. & MATAR, O.K. 2017 Reduced models for thick liquid layers with inertia on highly curved substrates. *SIAM J. Appl. Maths* **77** (3), 881–904.
- XUE, N., PACK, M.Y. & STONE, H.A. 2020 Marangoni-driven film climbing on a draining pre-wetted film. *J. Fluid Mech.* **886**, A24.
- XUE, N. & STONE, H.A. 2020 Self-similar draining near a vertical edge. *Phys. Rev. Lett.* **125** (6), 064502.
- XUE, N. & STONE, H.A. 2021 Draining and spreading along geometries that cause converging flows: viscous gravity currents on a downward-pointing cone and a bowl-shaped hemisphere. *Phys. Rev. Fluids* **6** (4), 043801.